Spring 2022

Mineralogy, Isotope Geochemistry and Geothermometry of the Lowry Deposit, Black Butte Copper Project, Meagher County, Montana

John Allard

Mineralogy, Isotope Geochemistry and Geothermometry of the Lowry Deposit, Black Butte Copper Project, Meagher County, Montana

by

John Allard

A thesis submitted in partial fulfillment of the
requirements for the degree of

Masters of Science in Geoscience
Geology Option

Montana Tech
2022

Abstract

The Black Butte Copper Project is a sedimentary rock hosted, Cu-rich massive sulfide deposit hosted in rocks of the ca. 1.5-1.325 Ga Mesoproterozoic Belt Supergroup. Copper-bearing sulfides, mainly chalcopyrite and tennantite, are hosted in debris flows, black shale, dolostone and sedimentary pyrite layers of the Newland Fm. of the Lower Belt Group in the Helena Embayment, an E-W striking limb of the greater NNW trending Belt Basin. Mineralization is hosted within two separate but contemporaneous deposits, Johnny Lee, which hosts Cu sulfides in an upper and lower sulfide zone within sedimentary pyrite and debris flow conglomerates, and Lowry, where Cu sulfides are hosted in a middle and lower sulfide zone in dolomite dissolution breccias and veins cutting the host Newland Fm. in addition to sedimentary pyrite and debris flows. Mineralization at Black Butte has many characteristics of sedimentary exhalative (sedex) type deposits- massive, laterally extensive pyrite hosted in black shales, accessory silver, formation within a continental rift, evidence of seafloor hydrothermal venting- but, unlike most sedex deposits, Black Butte is a Cu sulfide deposit that lacks Pb and Zn. Hence, the deposit model assigned to the Black Butte Project is a hybrid between sedex, based on the environment of ore formation, and stratabound sedimentary hosted Cu, based on the Cu dominant ore. This research aimed to apply robust and innovative geochemical methods to characterize the conditions of formation of the Lowry deposit. Sulfur stable isotope analysis of chalcopyrite from the Lowry deposit show a range of $\delta^{34}S$ between +/- 5‰ of zero. When plotted with other S isotopes of pyrite and chalcopyrite from the Black Butte Project, a broad range of S-isotope values in pyrite reflect bacterial reduction of marine sulfate (BSR), while the more restricted range in chalcopyrite can be explained by higher temperature thermochemical sulfate reduction (TSR). Carbonate isotopes from hydrothermal dolomite range from +16 to +22‰ in $\delta^{18}O$ and 0 to -5‰ in $\delta^{13}C$, and are depleted in both ^{18}O and ^{13}C compared to sedimentary carbonate from the Newland Fm. Bitumen occurs in recrystallized dolomite and veins along with quartz, pyrite and chalcopyrite, and has reflectance and Raman spectroscopy values consistent with maximum mean temperatures of 223± 8°C (n=8) with a range of 212.8 – 239.5°C and 247± 40°C (n=7) with a range of 219 – 265°C respectively. Sr isotopes from Lowry and Johnny Lee dolomite reflect the modeled Sr values for Proterozoic seawater. Pb isotopes of Lowry sulfides and dolomite plot within an upper crustal source.

These geochemical data, combined with observations of mineralized drill core through hand sample and microscopy, suggest that the Lowry deposit formed after deposition of the lower Newland Fm. at temperatures near or below 250°C. Limestone beds were altered to dolomite during diagenesis creating open space for hydrocarbon migration. High-temperature thermochemical sulfate reduction (TSR) replaced bacterial sulfate reduction (BSR) and altered hydrocarbons to bitumen and porewater sulfate to H_2S, creating favorable depositional sites for metalliferous fluids. Fluids were sourced from connate brines circulating in the Helena Embayment of the Mesoproterozoic Belt-Purcell basin that scavenged metals from an underlying crustal source and deposited sulfides and gangue upon encountering favorable facies while migrating along structural pathways.

Keywords: economic geology, hydrothermal ore deposits, Belt Supergroup, isotope geochemistry, Black Butte Copper Project

Dedication

This project was accomplished through a strong base of support, mostly my family and close friends, as well as many role models. To my wife, my family and my dear friends- thank you for your love, endless encouragement and patience. A special thanks to the many geologists whom I've had the privilege to interact with, their generous guidance has led me along an extremely rewarding path, and their enthusiasm has shown me that the work of a geologist is so much more than a career.

Acknowledgments

I would like to acknowledge the generous support from multiple societies and companies, and the individuals that volunteer their time to promote student involvement in economic geology, without whom this research would not have been possible- Society of Economic Geologists: Student Research Grant from the Hugh McKinstry Fund, Society for Mining, Metallurgy and Exploration: Stewart Wallace Memorial Scholarship, Tobacco Root Geological Society: Sibanye-Stillwater-Wheaton Precious Metals Scholarship, and Sandfire Resources America Inc.

Additionally, I would like to thank the many individuals whose assistance and feedback greatly improved the quality of this project- Jerry Zieg, Eric LeLacheur, and Adam Weist for providing the grounds for this study, never denying access to core-old and young-, manuscript reviews and financial and logistical support; Drs. Kaleb Scarberry and Todd Hoffman for their reviews of this manuscript; Dr. Paul Hackley and Javin Hatcherian for their guidance and efforts on reflectance analysis; Dr. Douglas Dvoracek for his guidance and efforts on radiogenic isotope analysis; and Drs. Simon Poulson, Ilya Bindeman and the staff at the University of Wyoming Stable Isotope Facility for their efforts on stable isotope analysis. Also, this work would not have been possible without the extensive documentation and research carried out by many geologists who have crossed paths with the Belt, Black Butte and economic geology in general.

Most importantly, I would like to acknowledge Dr. Chris Gammons for serving as a great mentor by providing unwavering guidance and patience, and for genuinely caring about his students; one of his greatest contributions to society is an extensive cohort of former students who better the world through their work in economic geology and environmental geochemistry.

Table of Contents

List of Tables

List of Figures

Thesis Statement

Sedimentary hosted copper deposits contain nearly one quarter of the world's known copper and are important sources of cobalt and silver (Singer, 1995). These deposits are typically high-grade and amenable to underground mining, leaving a much smaller environmental footprint than open-pit porphyry deposits. There are a few "supergiant" deposits (> 24 million metric tons contained copper) that rival or exceed large porphyry deposits in contained copper and average grade (Hitzman et al., 2005). Increased understanding of this deposit type and its variations will aid in future discoveries and increase the potential to significantly grow global copper reserves.

The Black Butte Project contains two copper resource areas, Johnny Lee and Lowry. A planned underground mine to exploit the high-grade Johnny Lee deposit has passed the permit stage, and development work is underway. While both resource areas are hosted in dolomitic shale of the Newland Fm, the deposits display different styles of alteration and mineralization. The Johnny Lee deposit (described in detail by Graham et al., 2012) hosts broad and continuous stratiform mineralization along sedimentary pyrite lithofacies, with little to no cross-cutting relationships, strong barite alteration in the hanging wall, and Sr-rich alteration in the footwall (Gammons and Zieg, 2014). In contrast, the Lowry resource has narrower intercepts with more cross cutting, vein-like mineralization, locally abundant bitumen, and intense carbonate (dolomite) alteration with unique textures. It is possible that epigenetic mineralization in the Lowry deposit represents a later-stage mineralizing event in the basin following burial and initial compaction and lithification. Using stable-isotope analysis and bitumen geothermometry, this study aims to characterize the Lowry deposit's ore-forming conditions.

Black Butte has been described as both a sedex deposit, and/or a sediment-hosted stratiform Cu deposit, strongly displaying characteristics of both deposit models. The Belt/Purcell Basin is host to numerous examples of both deposit types, and Black Butte may represent a hybrid of the two. A source for the mineralizing fluids remains unknown, but the Neihart Formation, a hematitic quartz-arenite that underlies the Newland host rocks by 200m, has been suggested as an aquifer for basinal brines and may be the metal source rock (White et al., 2014). In addition to stable isotopes of S, O, and C, this study employed Sr and Pb isotopes to see if the Neihart Fm. contains Sr and Pb that is isotopically similar to Sr-rich minerals (celestine, strontianite, dolomite) in the Black Butte deposits to evaluate the Neihart as a possible "redbed" metal source.

1. Introduction

1.1. Purpose and Scope

The Black Butte Copper Project (BBCP), formerly known as Sheep Creek, is a sediment hosted copper deposit located approximately 17 miles northwest of White Sulphur Springs, Meagher County, Montana (Figure 1) along the northern margin of the Helena Embayment of the Mesoproterozoic Belt-Purcell Basin. The deposit is unusual in that it has the geologic setting of a sedimentary-exhalative (SEDEX) deposit but a metal endowment typical of a sediment-hosted stratiform Cu deposit. Black Butte is hosted by the Newland Fm., a black shale/dolostone with interbeds of debris flow conglomerates. Two centers of Cu mineralization 2 km apart have been drilled on the property, termed the Johnny Lee and Lowry deposits. Multiple workers (Zieg and Lietch, 1998; Lydon, 2007; Graham, 2012; Graham et al., 2012; White et al., 2014; Present et al., 2017; Saintilan et al., 2021) have described Black Butte's sedimentary architecture, mineralization, stable isotopes and similarities to other deposits. The majority of previous work has focused on observations of the Johnny Lee Deposit, with the exception of Graham (2012) who included samples from four Lowry holes drilled circa 1987. The purpose of this study is to expand upon the geology, stable isotope geochemistry and thermal conditions at the Lowry Deposit in order to better describe its ore-forming fluids and metal source.

This chapter is an introduction to the regional and local geology of the BBCP and a description of its exploration history and current mine plan.

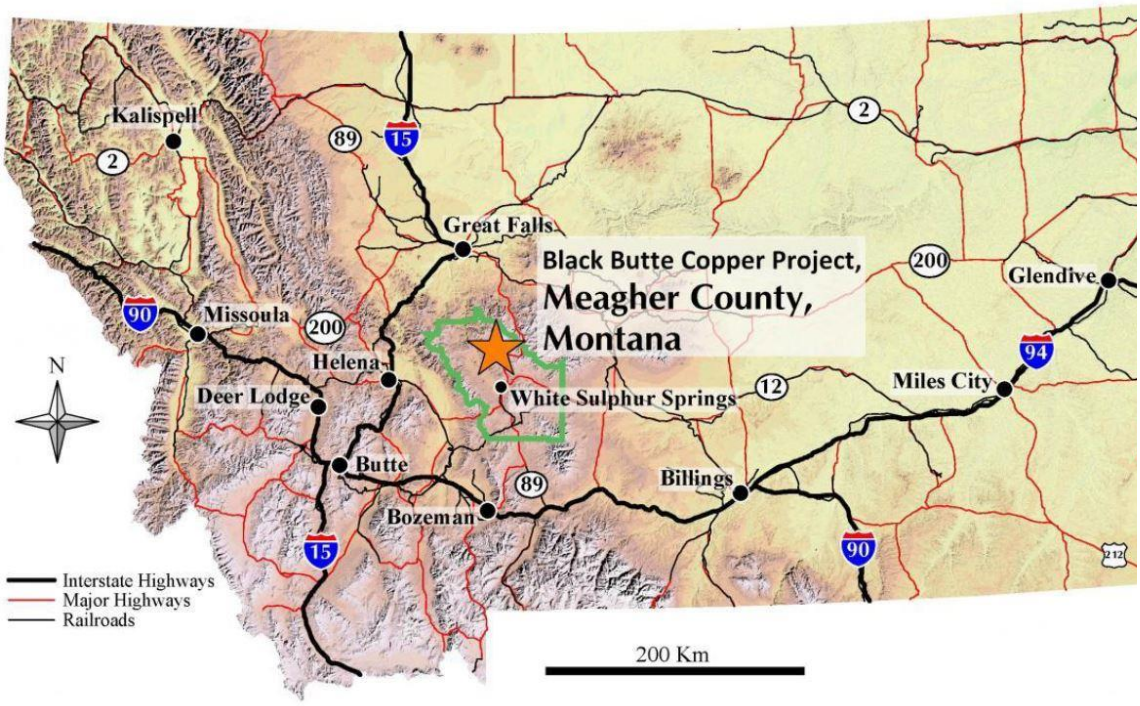

Figure 1: Location of Black Butte Copper Project. Courtesy of Sandfire Resources America Inc.

1.2. Geology of the Black Butte Copper Project

1.2.1. Regional Geology

1.2.1.1. The Belt Basin

The Belt Supergroup consists of siliciclastic and carbonate sedimentary rocks, and rift-related dikes and sills formed during the Mesoproterozoic from ca. 1.47 to 1.4 Ga (Anderson and Davis, 1995; Doughty and Chamberlain, 1996; Sears et al., 1998; Evans et al., 2000). The Belt-Purcell Basin formed as an intracontinental rift covering >200,000 km^2 and accumulated up to 20 km of marine to fluvial sediments in under 100 Ma (Winston and Link, 1993; Chandler, 2000; Evans et al., 2000).

The Belt Basin consists of an approximately 750 km long, NNW trending basin, as well as an E trending limb, the Helena embayment, at the SE margin of the main basin (Figure 2). The Helena embayment is bound by two regional structures, the Garnet Line to the north and the Perry Line to the south (Winston, 1986).

The rocks of the Belt Supergroup are split into four Groups, named from oldest to youngest respectively, the Lower Belt, Ravalli, Middle Belt Carbonate (a.k.a. the Piegan), and the Missoula (Figure 3). The Supergroup is host to several world-class base and precious metal deposits, including the Sullivan Ag-Pb-Zn SEDEX deposit, the Spar Lake, Rock Creek and Montanore sediment-hosted Cu-Ag deposits, and the Coeur d'Alene Ag-Pb-Zn vein deposits.

Whereas rocks along the western exposure of the Belt Supergroup have undergone at least three deformational events (Lydon, 2007 and references therein), and reached high-grade metamorphic conditions during the East Kootenay Orogeny (Doughty and Chamberlain, 1996), the northern margin of the Helena embayment in the Black Butte project area remains only weakly metamorphosed, and has experienced deformation primarily along reactivated Proterozoic structures during the Cretaceous to Paleocene Laramide Orogeny (Graham et al.,

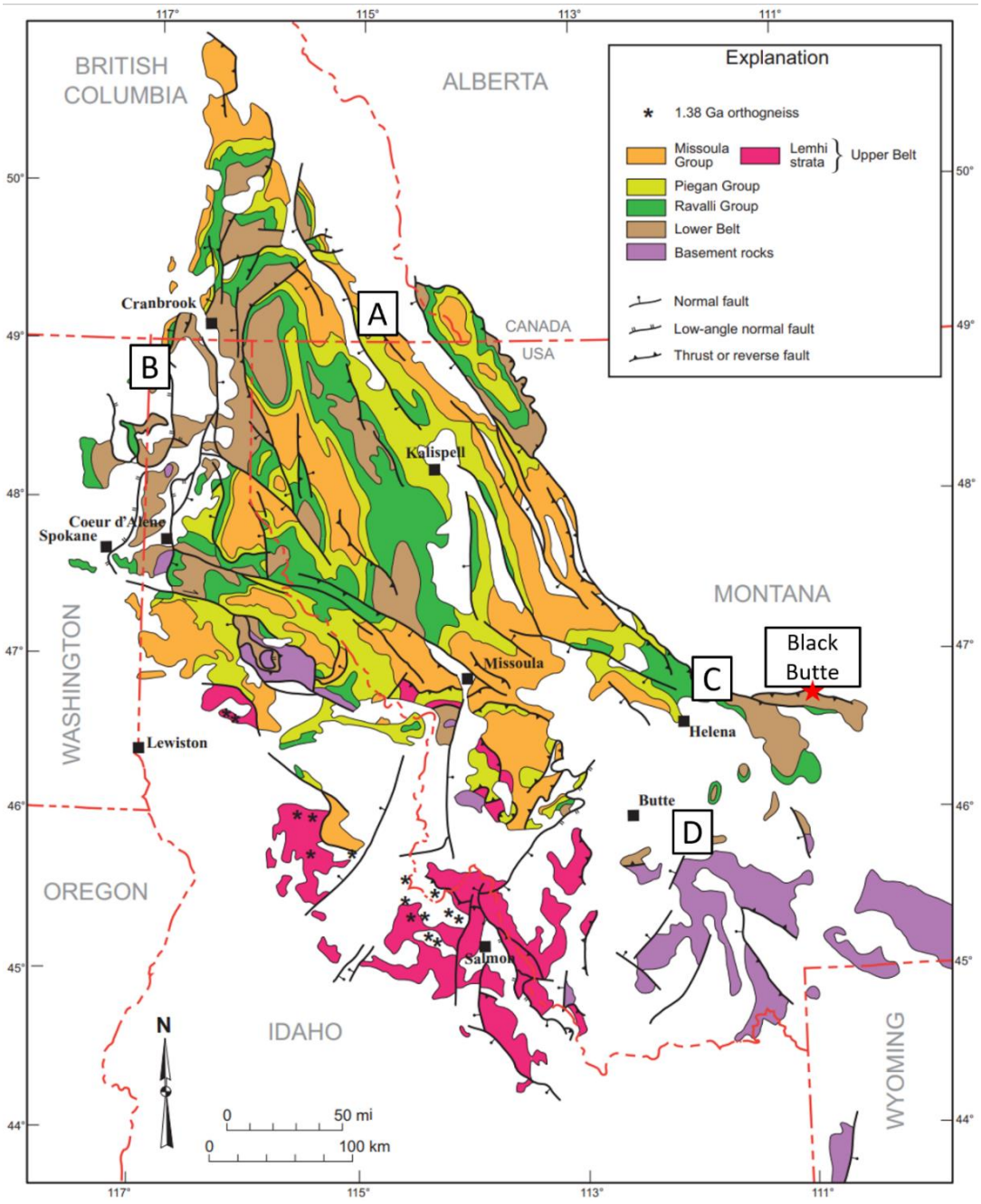

Figure 2: Current extent of Belt Supergroup outcrops from Lonn et al., 2020. Boxed letters correlate to stratigraphic columns in Figure 3.

2012). Additionally, Slotznick and others (2015) showed that the Newland formation at the Black Butte project area never experienced regional metamorphic conditions hotter than 200°C.

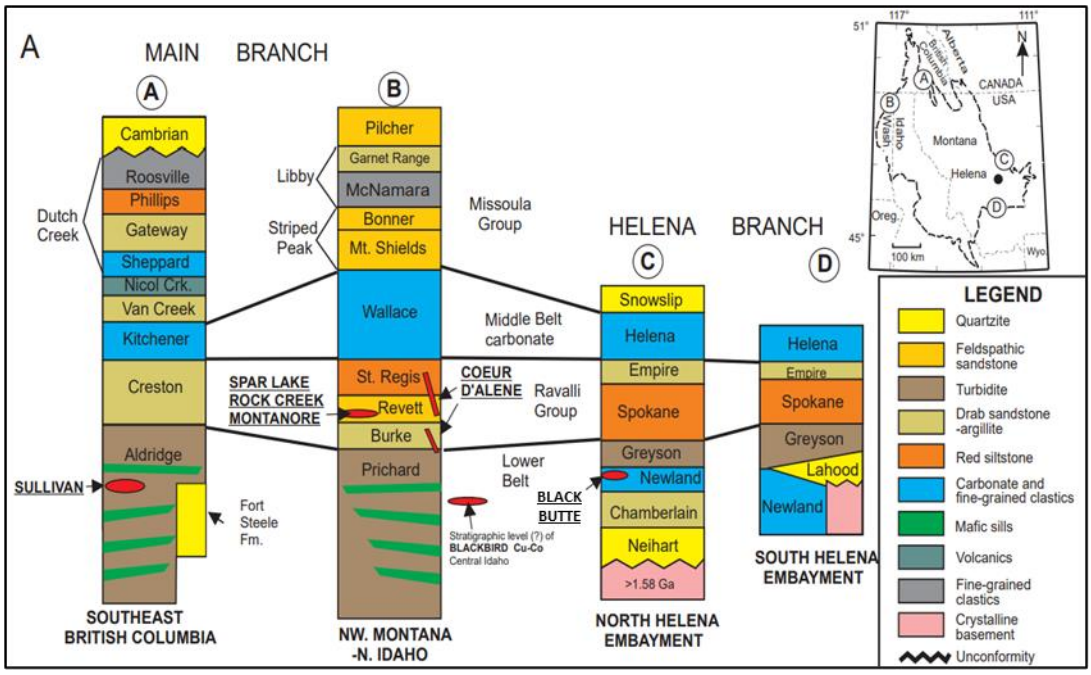

Figure 3: Stratigraphy of Belt Supergroups including groups, formations and major ore deposits. Section A represents names of Canadian Purcell formations correlated to the American Belt formations. From Lydon, 2007.

1.2.2. Local Geology

1.2.2.1. Stratigraphy

The Belt Supergroup at the Black Butte Project is limited to the Lower Belt Group, which unconformably overlies the Paleoproterozoic – Archean Basement (Figure 4). Belt rocks are unconformably overlain by Cambrian sedimentary rocks and are cut by Tertiary intrusions (Reynolds and Brandt, 2007).

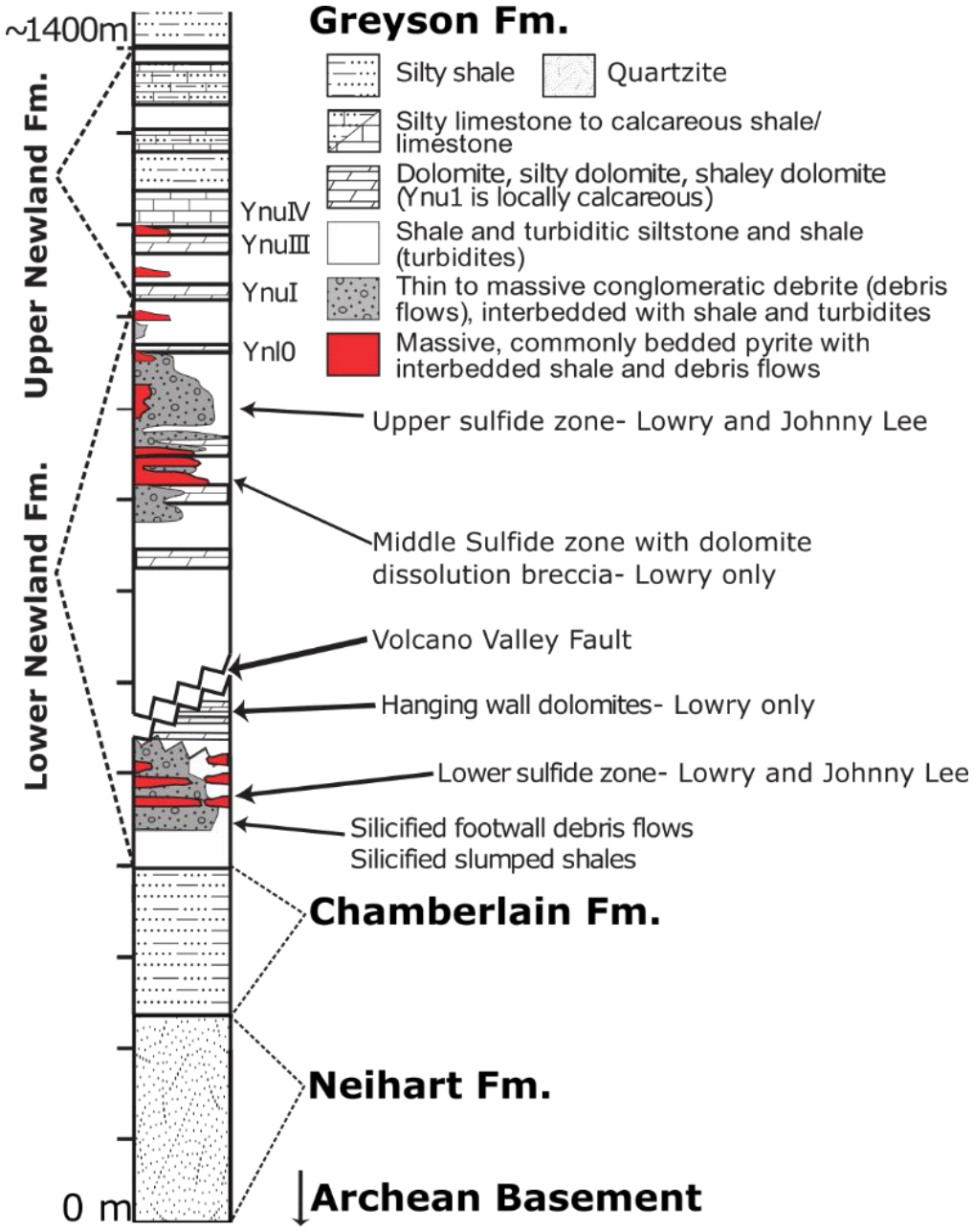

Figure 4: Stratigraphy of the Black Butte project area modified from Graham et al., 2012

The Neihart Formation (Yne) is 200-280m thick in the project area (Zieg, G.A., personal communication, September 2020) and was nonconformably deposited atop a 1.86 Ma granitic gneiss (Mueller et al., 2002) basement rock immediately prior to (Winston, 1989) or during (Schieber, 1989) the opening of the Belt Basin. The Neihart Fm. varies from a mature white

quartzite to an immature, hematite-mottled quartz-arenite with lenses of sand-pebble conglomerate and represents an aeolian to fluvial sheet sand deposited in a terrestrial environment prior to the marine inundation of the Belt Basin (Winston, 1989). The Neihart Fm. is a regionally extensive unit that has been correlated along the base of the Belt Supergroup across Montana and Idaho (Freeman and Winston, 1987; Winston, 1989); its type locality is approximately 25km NNE of the Black Butte project area.

The Neihart Fm. grades into the sandy to dolomitic shale of the Chamberlain Fm. (Yc), which is approximately 200 m thick in the project area (Zieg, G.A., personal communication, September 24th, 2020). The Chamberlain Fm. represents marine inundation of the Belt Basin and is interpreted as a near-shore mudflat environment (Godlewski and Zieg, 1984).

The Chamberlain Fm. grades into the Newland Fm. (Yn), a carbonaceous black shale with carbonate and debris flow interbeds, that is 1,100 m thick in the Black Butte area (Zeig, 1986) and is the host to copper mineralization at BBCP. The Newland Fm. is divided into upper and lower members, Ynu and Ynl respectively. The upper member is characterized by alternating shale and carbonate beds, while the lower member contains debris flow conglomerates and turbidite sequences which were likely shed from fault scarps during movement along basin-growth faults (Graham et al., 2012). Debris flow deposits dissipate, and the Newland Fm. thickens southward away from the Volcano Valley Fault, the major E-W bounding structure that cuts through the Black Butte project area.

The Newland Fm. is host to significant massive sulfide beds in the form of sedimentary pyrite, the formation of which was described by Present et al. (2018). Pyrite beds up to 90 m thick occur for at least 24 km along strike of the Volcano Valley Fault and for up to 8 km to the south (Zieg and Leitch, 1998).

In addition to the sedimentary rocks in the project area, Eocene dacitic dikes and sills are present in drill core at the Lowry and Johnny Lee, and in outcrop to the south of the Black Butte fault (Reynolds and Brandt, 2007) (Figure 5).

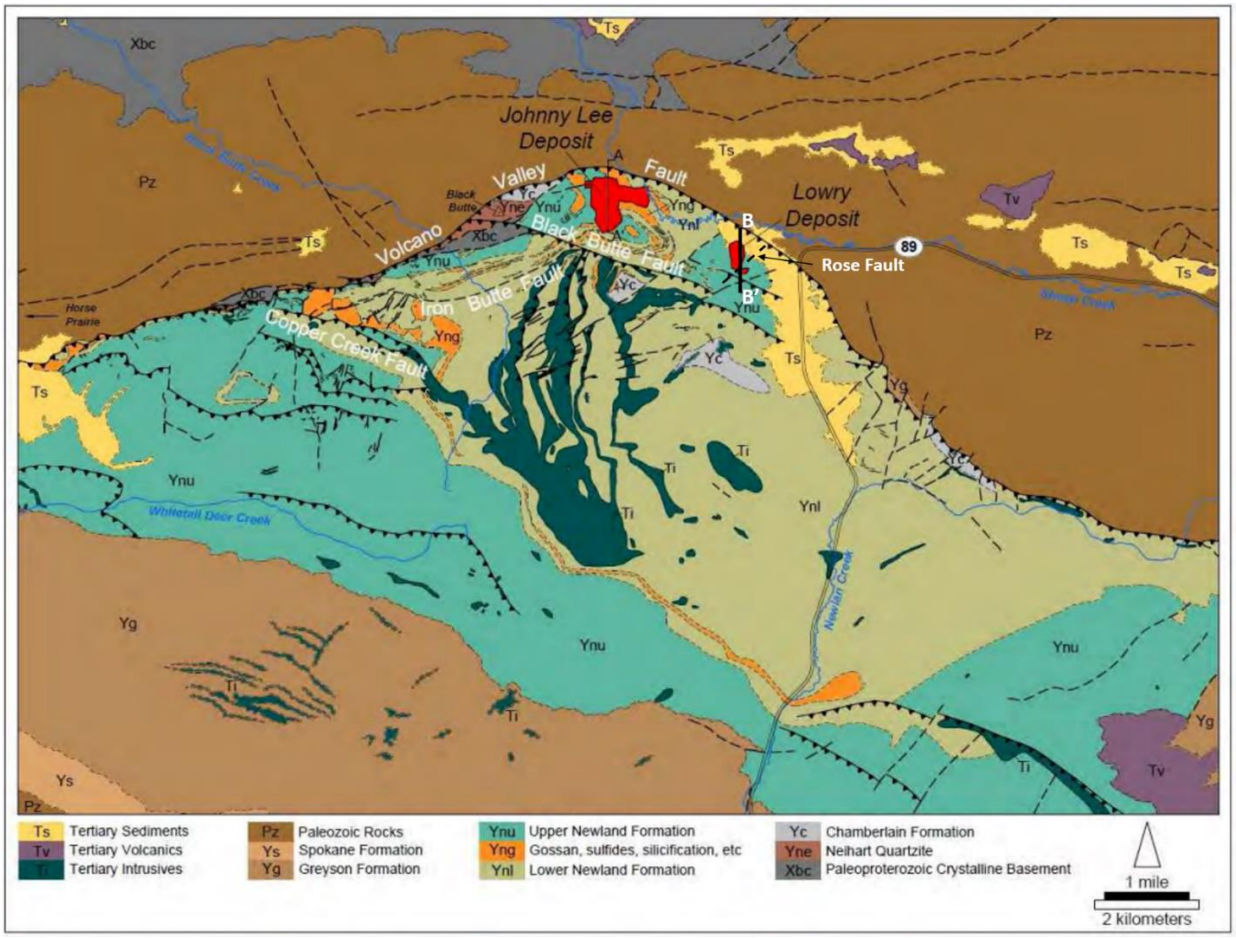

Figure 5: Surface geology of the Black Butte Copper Project from Zieg et al. (2013); The red areas represent the surface projection of the Johnny Lee and Lowry deposits. B-B' corresponds to Figure 7

1.2.2.2. Mineralization

Mineralization at BBCP occurs in two distinct deposits, Johnny Lee and Lowry (Figure 4). At Johnny Lee, two horizons are present with significant copper mineralization, the Upper Sulfide Zone (USZ) and the Lower Sulfide Zone (LSZ); at Lowry, there are three horizons with copper mineralization, the USZ, Middle Sulfide Zone (MSZ) and the LSZ (Figure 5). At both deposits, these layers are continuous within the Ynl stratigraphy but are fault-bounded in multiple directions. Although part of the same stratigraphic horizon, the USZ hosts much less copper mineralization at the Lowry deposit as opposed to the Johnny Lee deposit. The MSZ is present only at the Lowry, as well as its distinct dolomite alteration and style of copper mineralization, displaying much more veining than the mineralization at the Johnny Lee, which is typically bedding parallel. The LSZ occurs at both the Johnny Lee and Lowry deposits and is always beneath the Volcano Valley Fault.

The Lowry MSZ is the focus of this study. The Middle Sulfide Zone is so named because it lies stratigraphically below the USZ and structurally above the LSZ. When intact, the MSZ can measure approximately 80 m in thickness, stretching 750 m along a N-S axis, and 300 m across (E-W) (Figure 7).

1.2.2.3. Structure

Black Butte lies at the intersection of two major tectonic zones, the Lewis and Clark Tectonic Zone (LCTZ) (White, 2016) and the Proterozoic Great Falls Tectonic Zone (GFTZ), which separates the Archean Wyoming Craton from the Archean-Proterozoic Medicine Hat Craton (Gifford et al., 2018) (Figure 6).

The most significant structure in the project area is the Volcano Valley Fault (VVF), which makes a distinct arc at the site of the Black Butte deposits. The VVF has a net reverse

sense of offset, consistent with Sevier-age (late Cretaceous) compression, although it may have been reactivated as a normal fault since the Paleocene (Graham et al., 2012; Zieg et al., 2013). At the BBCP area, the VVF places Mesoproterozoic strata atop Cambrian sediments, and accommodated as much as 1 km of top-to-the-north reverse

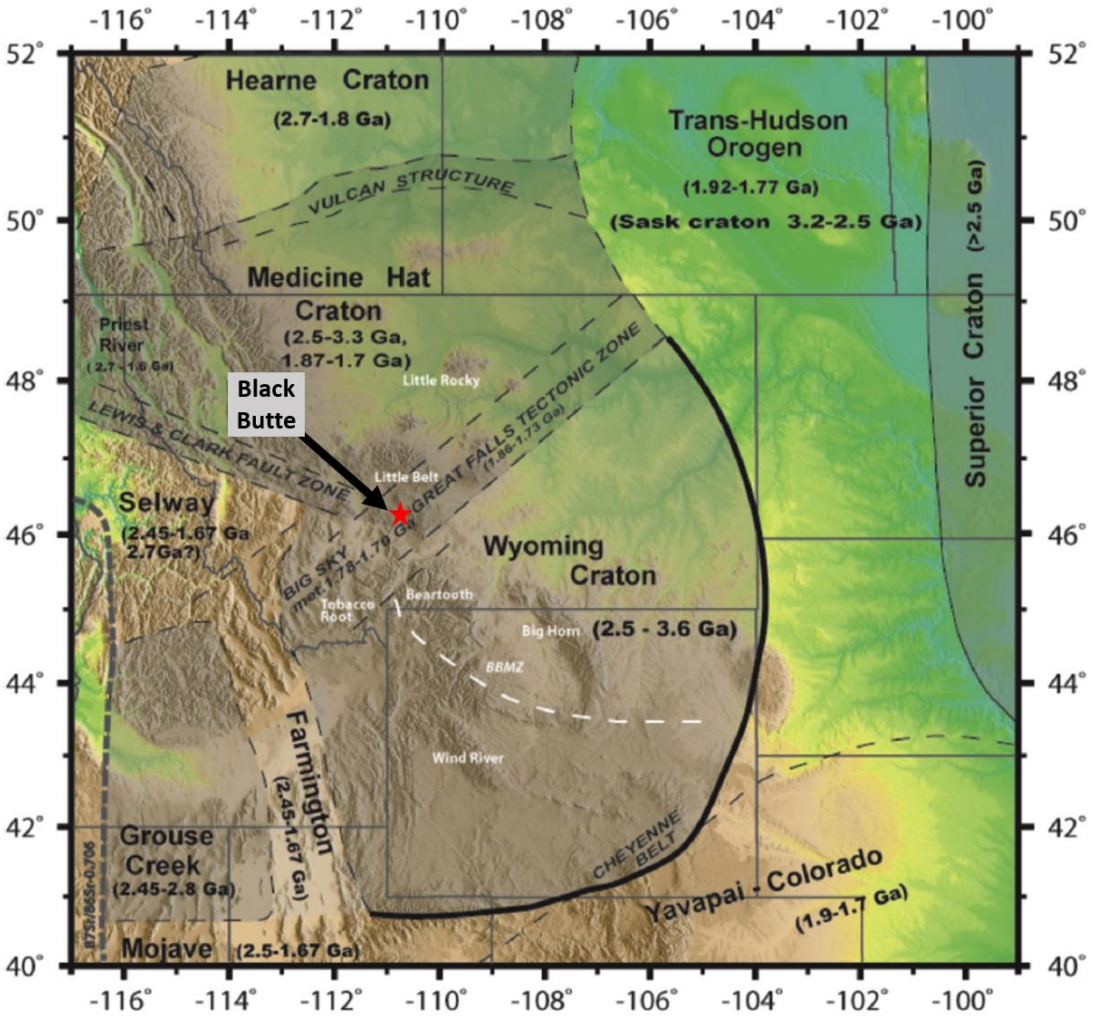

Figure 6: Tectonic map of Precambrian basement from Gifford et al., 2018. Note Black Butte's location along the intersection of the GFTZ with the LCTZ.

displacement (G. A. Zieg, pers. communication, December 2021) and approximately 1.6 km of left-lateral offset (Zieg et al., 2013).

As shown in Figure 7, the Black Butte deposits lie within both allochthonous and autochthonous blocks on either side of the VVF. At both the Johnny Lee and Lowry

deposits the LSZ lies below the VVF and is a part of the autochthonous block, while the USZ (Johnny Lee) and MSZ (Lowry) are within the allochthon. Both deposits are cut by numerous, high angle normal faults. The most significant high angle normal faults at BBCP include: 1) the E striking Buttress Fault in the Johnny Lee area, which is cut by the VVF and the Precambrian erosional surface and does not surface but is known through drilling to place Chamberlain Fm. above the lower Newland Fm.; and 2) the NE striking Rose Fault in the Lowry area, which cuts the Lowry deposit and VVF. Both the Buttress fault and Rose fault have been interpreted as Mesoproterozoic faults that accommodated basinal growth during the opening of the Helena Embayment and were reactivated during the Cretaceous to accommodate Laramide style compression (Graham et al., 2012; Zieg et al., 2013).

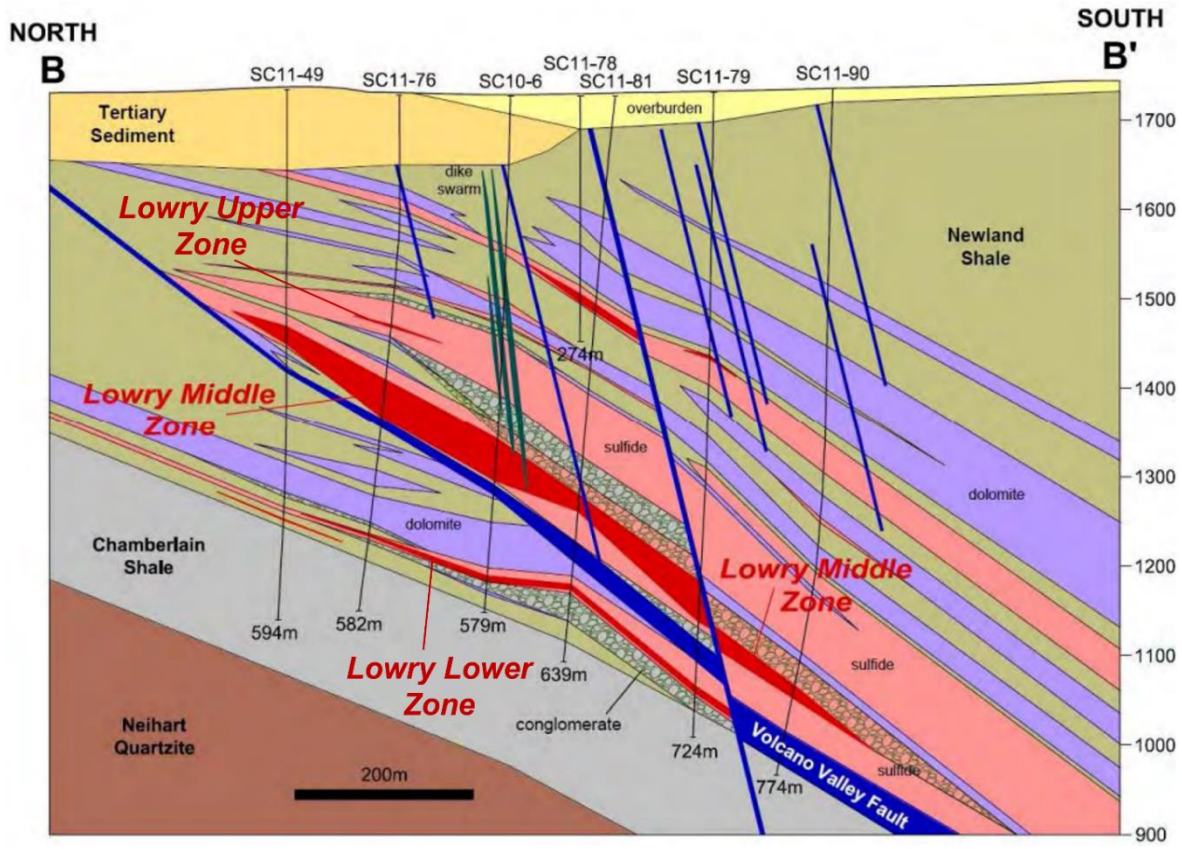

Figure 7: North-south cross section through the Lowry deposit looking east. Adapted from Zieg et al. (2013). Blue lines represent high angle normal faults with minor offset, green lines are Tertiary dikes, pink units are massive pyrite, red units are Cu-mineralized massive sulfide.

1.2.3. Mineral Resources

The Johnny Lee deposit was discovered in 1985 during a joint venture between Cominco American and BHP. The project has been owned by multiple mining companies since its discovery. At the time of this thesis, BBCP is owned by Sandfire Resources America Inc. (Sandfire). Sandfire became the majority shareholder of the BBCP in 2014 through purchase agreements with Tintina Resources, the project owner and operator at the time.

The BBCP is host to low tonnage, high-grade deposits that will be mined underground using cut and fill. The mine plan for the Johnny Lee deposit was permitted in

April of 2020 (MT DEQ, 2020). The mineral resource estimates for the Johnny Lee and Lowry deposits as of 2019 and 2020 respectively are listed in Tables 1 and 2.

The Lowry deposit is currently in the pre-feasibility stage and is not permitted under the 2020 Mine Operating Permit.

Table 1: Johnny Lee deposit mineral resource estimate as of October 15, 2020, from Malhotra et al. (2020).

Category	Quantity (Mt)	Cu (%)	Total Metal (kt)
UCZ			
Measured	1.4	2.6	36.2
Indicated	8.3	2.3	191.3
Measured and Indicated	9.7	2.4	227.5
Inferred	2.2	2.2	49.5
LCZ			
Measured	0.6	5.7	32.9
Indicated	0.6	7.9	50.5
Measured and Indicated	1.2	6.8	83.4
Inferred	0.5	6.3	30.3
Combined UCZ + LCZ			
Measured	2.0	3.5	69.1
Indicated	8.9	2.7	241.8
Measured and Indicated	10.9	2.9	310.9
Inferred	2.7	3.0	79.7

Table 2: Lowry deposit mineral resource estimate as of October 15, 2020, from Malhotra et al. (2020).

Category	Quantity (Mt)	Cu (%)	Total Metal (kt)
LMCZ			
Inferred	5.7	2.53	318.7
LLCZ			
Inferred	2.6	2.13	121.3
Combined LMCZ + LLCZ			
Inferred	8.3	2.41	440.0

2. Methods

2.1. Sample Collection

Over seventy samples were collected between October 2020 and May, 2021 of representative intercepts from nine angled drill holes that intersected the Lowry sulfide zones

along N-S and E-W transects. Sulfides, gangue minerals and representative host rock were sampled from each hole. Samples were selected for isotope analysis, bitumen reflectance analysis and reflected light microscopy. Samples were described, photographed, and analyzed with a Niton portable X-ray fluorescence (pXRF) instrument to screen for metal content. An additional eight samples were collected from the Johnny Lee USZ and LSZ in August 2012 for $\delta^{13}C$, $\delta^{18}O$ and Sr isotope analysis during the study of Gammons and Zieg (2014) (Appendix A).

All depths reported in this study are drill depths from angled drill holes, not absolute depth from surface.

2.2. Reflected Light Microscopy

Samples were chosen for reflected light microscopy based on sulfide and gangue mineralogy and textures. One-inch diameter plugs were cut from drill core sample, set in epoxy, and polished using a Buehler Automet polisher with grit sizes from 75 to 0.25 microns at Montana Technological University (MTU). The samples were examined on a Leica CM 2700 P polarizing microscope and photomicrographs were taken with a Leica MC170 HD camera to record ore and gangue textures.

2.3. Stable Isotopes

Samples with coarse-grained chalcopyrite, pyrite, anhydrite, dolomite, and quartz were selected for stable-isotope analysis. Mineral separates were taken from multiple textures using a Dremel with a tungsten-tipped bit. All sulfide and carbonate minerals separated for isotopic analysis were analyzed by an Olympus Terra portable X-ray diffractometer (p-XRD) at the MTU campus, which uses a cobalt radiation source. Separates were ground to -100 mesh and scanned for 45 minutes in the pXRD. The scanning chamber was cleaned following each separate. Diffractograms were interpreted using *XPowder* software, supplied by the vendors.

2.3.1. Sulfur Isotopes

Chalcopyrite (n=13) and pyrite (n=1) separates were sent to the University of Nevada Reno for $\delta^{34}S$ analysis by Dr. Simon Poulson. Analysis used a Eurovector elemental analyzer interfaced to a Micromass Isoprime stable isotope ratio mass spectrometer (IRMS) after the methods of Giesemann et al. (1994) and Grassineau et al. (2001). Data are reported as $\delta^{34}S$ in the usual ‰ (per mil, or parts per thousand) notation relative to the Vienna Canyon Diablo Troilite (VCDT) isotopic standard and have an estimated uncertainty of ± 0.1‰.

2.3.2. Carbon and Oxygen Isotopes

Mineral separates were collected from samples with hydrothermal carbonate gangue, including dolomite, strontianite ($SrCO_3$) and celestine ($SrSO_4$), as well as one dolomitic shale sample from the Newland Fm. Seven of the twenty-six samples were collected in August 2012 (see Appendix A), and the remainder were collected during sampling events between October 2020 and May, 2021.

$\delta^{13}C$ and $\delta^{18}O$ analysis of dolomite and strontianite were performed at the Stable Isotope Facility (S.I.F.) at the University of Wyoming. The $^{13}C/^{12}C$ composition of carbonates was determined by acidification of the samples with 99.99% phosphoric acid. The method used 12mL headspace vials as the vessel for acidification in conjunction with a gas chromatograph, which was coupled to an isotope ratio mass spectrometer in continuous flow mode. The head space vials that contained the samples were flushed with helium. After flushing, 100µL of the phosphoric acid was injected into each vial. The samples were placed on the bench top at room temperature and allowed to react for 24 hours. After the reaction was complete, a sample of the headspace air was injected onto the gas chromatograph column for gas separation and isotopic analysis.

Quality assessment of carbon and oxygen isotope composition of carbonates was based on the standard uncertainty of the known value of the secondary laboratory reference material calculated on multiple analyses. For carbon isotope composition, if the standard uncertainty was greater than 0.15‰, the unknowns were re-analyzed (until the 2-sigma expanded standard uncertainty of the result was better than 0.3‰).

The carbon isotopic composition is reported in ‰ (per mil, or parts per thousand) relative to the Vienna Pee Dee Belemnite (VPDB) isotopic standard such that NBS 18 calcite, NBS19 TS-limestone, and LSVEC lithium carbonate, respectively are -5.01‰, +1.95‰, and -46.6‰. For oxygen isotope ratio composition, if the standard uncertainty was greater than 0.2‰, the unknowns were re-analyzed (until the 2-sigma expanded standard uncertainty of the result is better than 0.4‰). The oxygen isotopic composition is reported in per mil relative to VPDB scale such that NBS 18 calcite, NBS19 TS-limestone, and LSVEC lithium carbonate, respectively are -23.2‰, -2.2‰, and -26.7‰. Values of $\delta^{18}O$ vs. VPDB were recalculated to VSMOW using conversion factors in Clark and Fritz (1997).

2.3.3. Carbon of Bitumen

Three samples of bitumen from the Lowry deposit were separated for C-isotope analysis. Approximately 2 to 4 mg of each sample were weighed into a cup made of tin foil. The samples, along with 3 laboratory standards (calcite, $\delta^{13}C$ = -16.26‰; KH-phthalate, $\delta^{13}C$ = -28.78‰; NaHCO3, $\delta^{13}C$ = -6.38‰), were analyzed using a carbon combustion chamber and a Picarro Cavity Ring-Down (CRD) analyzer at MTU. The C-isotopic composition of the laboratory standards were previously cross-checked vs. USGS-40 ($\delta^{13}C$ = -26.39‰) and USGS-41 ($\delta^{13}C$ = +3.0‰) reference standards. The $\delta^{13}C$-bitumen values are reported relative to VPDB and have an estimated uncertainty of ± 0.2‰.

2.3.4. Oxygen of Quartz

Samples of vein quartz were broken and examined under a binocular microscope to select fragments ~ 2mm in diameter that were optically clear and devoid of mineral inclusions. The fragments (5 to 10 per sample) were rinsed with water, dried, placed in a vial, and sent to the University of Oregon for isotopic analysis by Dr. Ilya Bindeman. A 35 W CO_2 laser line coupled with MAT 253 10 kV gas source isotope ratio mass spectrometer (IRMS) using purified BrF_5 reagent was used. Gasses generated during the fluorination reaction were purified using liquid N_2 cryogenic traps and a Hg diffusion pump before released oxygen was converted to CO_2 using a platinum–graphite filament. Gore Mountain Garnet (UOG, accepted $\delta^{18}O = 6.52$ ‰) was analyzed 4 times per analytical session to correct data on SMOW scale and for day-to-day variations with an average correction of about −0.2 ‰. Overall long-term precision of UOG repeat analyses normalized to each day of analysis was 0.08 ‰ (2σ, n = 25). Yields were measured by a Baratron gauge and were close to 100% (note 100% for quartz is 16.65 mols/mg of O_2 gas). The final $\delta^{18}O$ values are reported relative to the Vienna Standard Mean Ocean Water (VSMOW) isotopic standard and have an estimated uncertainty of ± 0.1‰.

2.4. Radiogenic Isotopes

2.4.1. Sample Selection

Radiogenic isotopes of Pb and Sr were used to compare ore and gangue minerals to potential source rocks. The use of Sr and Pb as metal-tracers is a technique that has been applied successfully in many studies of hydrothermal ore deposits (Potra & Moyers, 2017; Potra et al., 2018; Gigon et al., 2020), including some hosted by the Belt Supergroup (Beaudoin, 1997). The technique relies on the inference that Pb and Sr, either as major or trace elements, were derived

from the same metal source as the ore minerals and were transported and deposited by the same fluid (Tosdal et al., 1999; Champion and Huston, 2016).

For this study, Pb was analyzed from chalcopyrite and sparry dolomite sampled from the Lowry MSZ and LSZ, and from bulk rock samples from the Chamberlain and Neihart fms. underlying the Newland fm.; Sr was analyzed from sparry dolomite sampled from the Lowry MSZ and LSZ, from bulk rock samples from the Chamberlain and Neihart fms. and from strontianite, barite and dolomite from the Johnny Lee USZ and LSZ. Johnny Lee samples were collected during a separate sampling campaign in August 2012 (Gammons and Zieg, 2014), were prepared at MTU and were analyzed at the University of Waterloo. The mineral separates (chalcopyrite, dolomite) and bulk rock samples from the 2020-2021 sampling campaigns were prepared at MTU and sent to the Center for Applied Isotope Studies (CAIS) at the University of Georgia for the isotope analysis described in sections 3.4.2-3.4.5 below.

Additionally, select bulk-rock samples were analyzed by ICP-MS at CAIS for total Rb and Sr content.

2.4.2. Sample dissolution

All sample preparation (except pulverizing and weighing) was done in a class 1000 or 100 cleanroom area at the University of Georgia Institute for New Materials Research; all reagents used were Optima- or Suprapure-grade, and all water was 18 mega-ohm Millipore.

The entire volume of sample (as received) was pulverized in a pre-cleaned and pre-contaminated hardened steel puck-and-ring shatterbox. Pulverized material was homogenized by shaking, then repeatedly splitting, until approximately 100 mg remained.

Between 50-100 mg of this material was weighed into cleaned Savillex beakers and digested for 3 days in a mixture of HF-HNO_3-$HClO_4$. Each day the Savillex beakers were removed from the hotplate and sonicated for around 30 minutes to promote dissolution,

After 3 days, beakers were opened and allowed to evaporate until incipiently dry, then taken back up into 8N HNO_3, capped, and allowed to digest again on the hotplate overnight. Individual beakers were then opened and brought to incipient dryness. Each dried sample bead was then taken into solution in 1 mL of 8M HNO_3 and allowed to dry on the hotplate; this process was repeated a second time. In each step, it is important to avoid over-drying the residual bead. The final bead was then taken up in 250 microliters of 1M HBr for column separation of Pb and Sr, in that order.

2.4.3. Column separation of Pb & Sr: general procedure

Both Pb and Sr were separated from the same initial 100 mg split taken from any individual sample. The details are described below, but generally speaking, it is done by collecting the first 3 mL of waste eluent after loading the sample on the Pb columns; this fraction contained the Sr, which was not retained by the Pb-collecting resin. This 3mL aliquot was then dried down, converted to nitrate form, taken into solution in HNO_3, and processed on Sr-collection columns, separate from the Pb columns.

2.4.4. Pb Analysis

Pb was separated from dissolved rock powders using Dowex 1-8X (100-200 mesh) resin, following the methods described in Simbo et al. (2019).

Immediately prior to analysis, all samples and standards were spiked with a Tl solution (Pb:Tl approx. 4:1) for mass-fractionation correction. Throughout the data collection process, NBS 981 Pb standard was run before and after each sample to monitor instrument stability and to

accommodate normalization to published values of NIST 981 (see below). All results were corrected for isobaric interference from 204Hg (which was always negligible), then empirically normalized using the exponential law for mass bias correction using $^{205}Tl/^{203}Tl = 2.3875$ (Belshaw et al., 1998).

The values measured for unknowns were corrected by the standard-sample bracketing method of Weis et al. (2006) and White et al. (2000) using the NIST-981 values of Baker et al. (2004): ($^{208}Pb/^{204}Pb = 36.7262$; $^{207}Pb/^{204}Pb = 15.500$; $^{206}Pb/^{204}Pb = 16.9416$; $^{208}Pb/^{206}Pb = 2.16781$; and $^{207}Pb/^{206}Pb = 0.91491$) to compensate for instrumental drift and to aid in interlaboratory comparison. The values for these same ratios, measured over the course of the analyses, were, in respective order (n=38); 36.740±0.009; 15.505±0.003; 16.948±0.004; 2.16785±0.00026; and .91487±0.00013.

2.4.5. Sr Analysis

Sr was separated from dissolved rock powders by standard ion chromatographic processing using Sr-Spex resin from Eichrom, following detail developed by Scher et al. (2014). $^{87}Sr/^{86}Sr$ ratios were corrected for mass bias using exponential law and $^{86}Sr/^{88}Sr = 0.1194$. ^{87}Sr was corrected for the presence of Rb by monitoring the intensity of ^{85}Rb and subtracting the intensity of ^{87}Rb from the intensity of ^{87}Sr, using $^{87}Rb/^{85}Rb = 0.386$ and a mass-bias correction factor determined from $^{86}Sr/^{88}Sr$. All analyses were done using on-peak measured zeros determined on an ultra-high purity 2% HNO_3 solution to correct for isobaric interferences of Kr impurities in the Ar gas. The $^{87}Sr/^{86}Sr$ value measured for NBS 987 during the course of running these samples was 0.710229 ± 0.000025 (n=6).

2.5. Bitumen Reflectance

Bitumen reflectance is a widely applied method used to constrain hydrocarbon reservoir maturity (Hackley et al., 2018). Like vitrinite, the reflectivity of solid bitumen increases with increasing thermal maturity. This relationship can be used to estimate the peak temperature experienced by solid bitumen (Riediger, 1993; Barker and Bone, 1995; Landis and Castano, 1995; Hackley et al., 2020).

Polished plugs were made of bitumen in-situ and from bitumen separates collected from veins. Plugs were mounted and polished at MTU and bitumen content was confirmed under a reflected light microscope. Samples were then sent to the USGS Organic Petrology Lab in Reston, Virginia for reflectance analysis by Mr. Javin Hatcherian.

A Leica DM4000 microscope equipped with LED illumination and monochrome camera detection was used for reflectance analysis with the computer program DISKUS-FOSSIL by Hilgers Technisches Buero with a N-LASF46A (1.312) calibration standard from Klein and Becker.

QA/QC in the USGS Organic Petrography Laboratory (OPL) is conducted utilizing a quarterly round-robin exercise, to ensure repeatability between reflectance measurements in the OPL and other organic petrography laboratories. Analysts working in the OPL are commonly accredited by the International Committee on Coal and Organic Petrography to assess analyst capability. Mr. Hatcherian performed the analysis, and his accreditation is available online (ICCOP.com, 2021).

2.6. Raman Spectroscopy of Carbonaceous Material

Raman spectroscopy is a rapid, non-destructive analytical technique with many uses, including mineral identification and thermal maturity analysis. Raman spectroscopy of

carbonaceous materials (RSCM) is used for calculating the peak temperature experienced by carbonaceous (organic) material (Henry et al., 2019 and references therein). RSCM has been applied to structural problems to calculate maximum heating along fault zones (Furuichi et al., 2015), regional and contact metamorphism to constrain peak burial depth and metamorphic temperatures (Beyssac et al., 2002a, 2002b), and to thermal studies of shales to constrain reservoir maturity (Hackley and Lunsdorf, 2018; Lupoi et al., 2019).

For this study, peak temperature estimates for bitumen were calculated using bitumen reflectance analysis (Section 4.4). To confirm the results of bitumen reflectance analysis (Section 4.4), RSCM was applied to a subset of the bitumen samples to calculate their peak temperature.

Bitumen samples were analyzed in one-inch diameter polished plugs using a Renishaw Raman microscope equipped with a 514 nm (green) laser at the MTU Center for Advanced Materials Processing (CAMP). For bitumen, 15-18 spots were analyzed randomly across multiple grains, and was analyzed three times for 3 seconds per acquisition at 10% intensity. Spectra results were processed using the Iterative Fitting of Raman Spectra (IFORS) software (Lünsdorf and Lünsdorf, 2016), which was accessed from http://www.sediment.uni-goettingen.de/download/. IFORS uses curve fitting to calculate the scaled total area (STA) under the D and G band. STA is then used to calculate peak temperature using the calibration curve of Lünsdorf and Lünsdorf (2016), with uncertainties ranging from 36-40°C per spot. A mean temperature was calculated from the range of spot temperatures for each sample.

3. Results

3.1. Sulfide and Gangue mineralogy

3.1.1. Sulfide Mineralogy

This section will describe the ore-stage sulfides observed in the Lowry deposit. For detailed description of the pre-ore sedimentary pyrite and net-textured pyrite, see Present et al. (2017). Sulfide mineralization at Lowry occurs dominantly as chalcopyrite and pyrite with lesser, typically fine-grained inclusions of tennantite, sphalerite and galena. Cu-bearing sulfides commonly occur in multiple textural forms that are distinct from textures reported for the Johnny Lee deposit (Graham et al., 2012; White, 2012; Zieg et al., 2013). Multiple styles of mineralization textures most common in the Lowry deposit, specifically the MSZ of the Lowry, are described below.

- 1-10 cm chalcopyrite and pyrite +/- tennantite veins cutting the host lower Newland Fm. are common throughout the copper mineralized MSZ (Figure 8. A, B)
- Dolostone dissolution breccias with mono to polylithic clasts in a matrix of sparry white (Figure 11. B) dolomite replaced or infilled by chalcopyrite and pyrite (Figure 8. D). Bitumen and quartz are common accessories to the dolomite dissolution breccias. Dissolution breccias are a laterally extensive subunit within the lower Newland Fm. in the area of the Lowry deposit. In hand sample and polished section, copper sulfides appear intergrown (coeval) with sparry dolomite, but it is possible that the copper sulfides grew later than the dolomite gangue as void-fill.
- Chalcopyrite and late pyrite surrounding and replacing sedimentary pyrite in net-textured pyrite, bedded pyrite and pyrite clasts in debris flow conglomerates (Figure 8. C). Polished plug microscopy revealed that the majority of the early, sedimentary

pyrite (bedded) or net-texured pyrite observed in the Lowry MSZ is surrounded by later copper sulfides and pyrite, little evidence of replacement was observed.

- Replacement of debris-flow matrices or infill of pore spaces

Figure captions include drill hole numbers and sample drill depths (meters) for each photo (SC##-###-###. ##(m)).

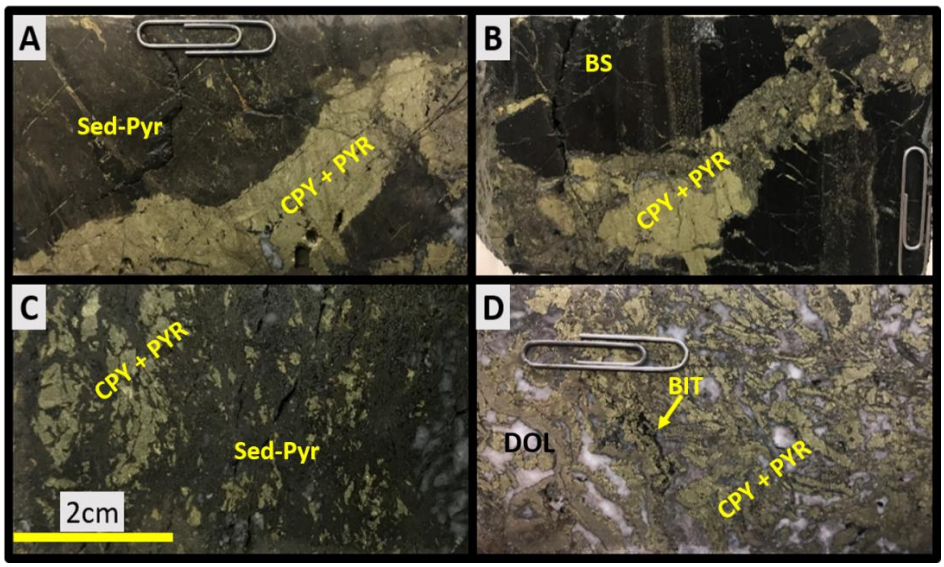

Figure 8: Lowry sulfide textures- A- SC12-157-416.72, B- SC12-163-457: chalcopyrite-pyrite +/- tennantite veins cutting black shale and sedimentary pyrite in the lower Newland Fm.; C- SC12-154-372.08: chalcopyrite and sedimentary pyrite in net texture; D- SC12-154-372.08- chalcopyrite, pyrite and bitumen replacing or infilling crustiform dolomite. Bit- bitumen, bs- black shale, cpy- chalcopyrite, dol- dolomite, sed-pyr- sedimentary pyrite, pyr- pyrite.

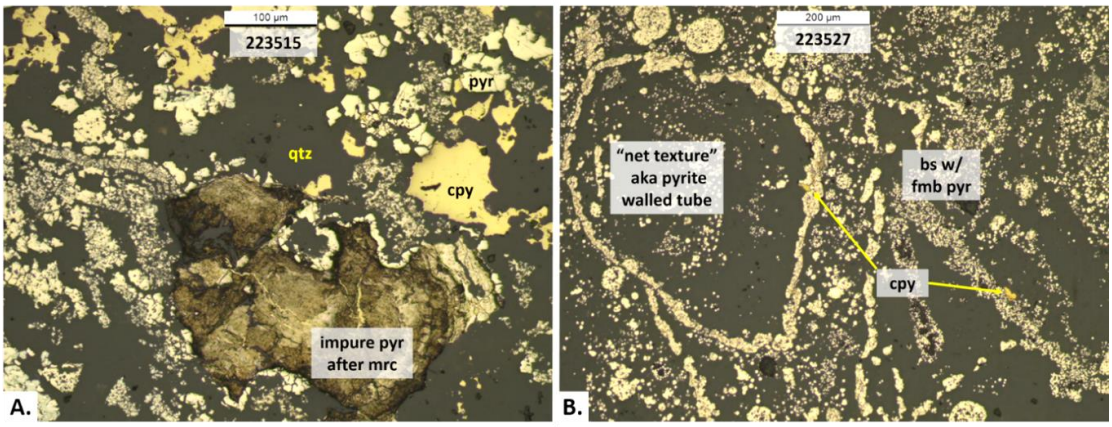

Figure 9: Reflected light photomicrographs of common pyrite textures from the Lowry MSZ- A- SC12-154-385.77: chalcopyrite and pyrite in quartz with early impure pyrite after crustiform marcasite; B- SC12-157-428.19: pyrite framboids and net texture, referred to by Present et al. (2018) as "pyrite walled tube structures", with chalcopyrite in black shale of Ynl. Bs- black shale, cpy- chalcopyrite, fmb- framboidal, mrc- marcasite, pyr- pyrite, qtz- quartz.

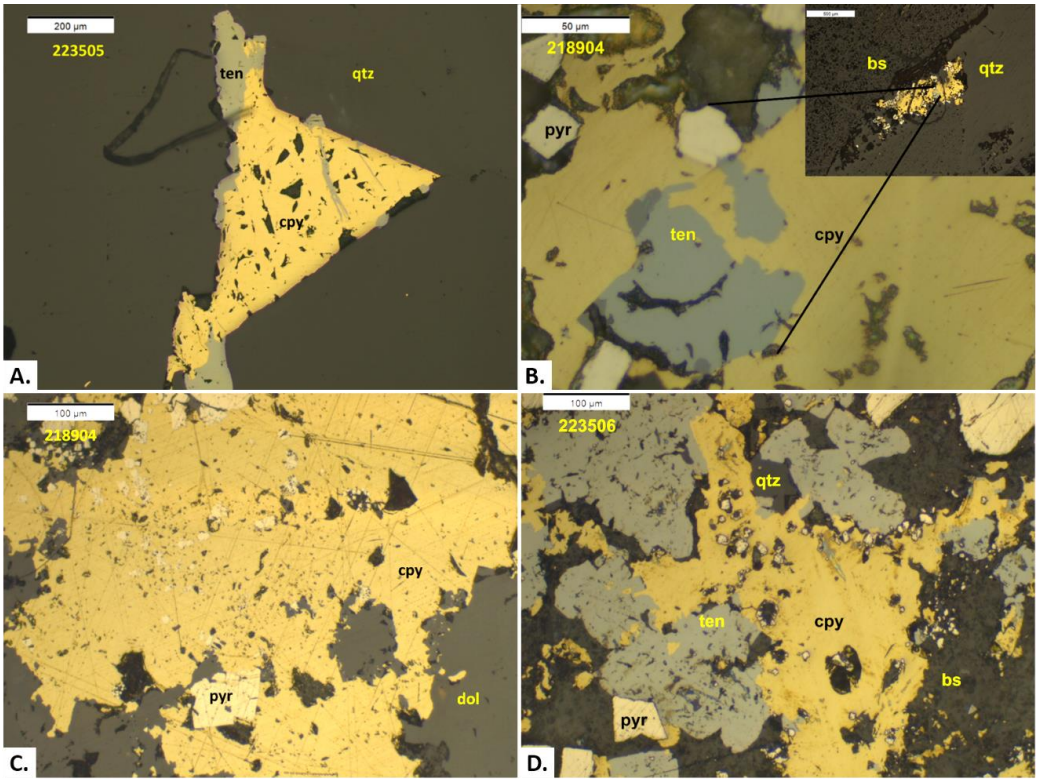

Figure 10: Reflected light photomicrographs of common chalcopyrite textures from the Lowry MSZ- A- SC12-160-415.15: Chalcopyrite and tennantite in a quartz breccia; B, C- SC12-168-351.22: pyrite, tennantite and chalcopyrite along margin of quartz-dolomite and black shale clast; C: pyrite and chalcopyrite in crustiform dolomite; D- SC12-160-414.3: pyrite, tennantite and chalcopyrite along margin of chalcopyrite-pyrite vein and shale. Bs- black shale, cpy- chalcopyrite, dol- dolomite, pyr- pyrite, ten- tennantite.

3.1.2. Gangue Mineralogy

Copper mineralization in the Lowry deposit is strongly associated with white sparry dolomite and lesser quartz veins and broad silicification of host rock, which can be observed in hand sample. Sparry dolomite, also described as baroque or saddle dolomite, is a common alteration product of the Newland Fm. at the Lowry. Dolostone in the Newland Fm. was locally recrystallized as crustiform dolomite and dissolution breccia and cut by dolomite veins. Crustiform textures are inferred to be the result of local recrystallization in places where grain size and color are zoned relative to dolostone, fining from coarse, white centers to darker grey recrystallized dolostone (Figure 11, A).

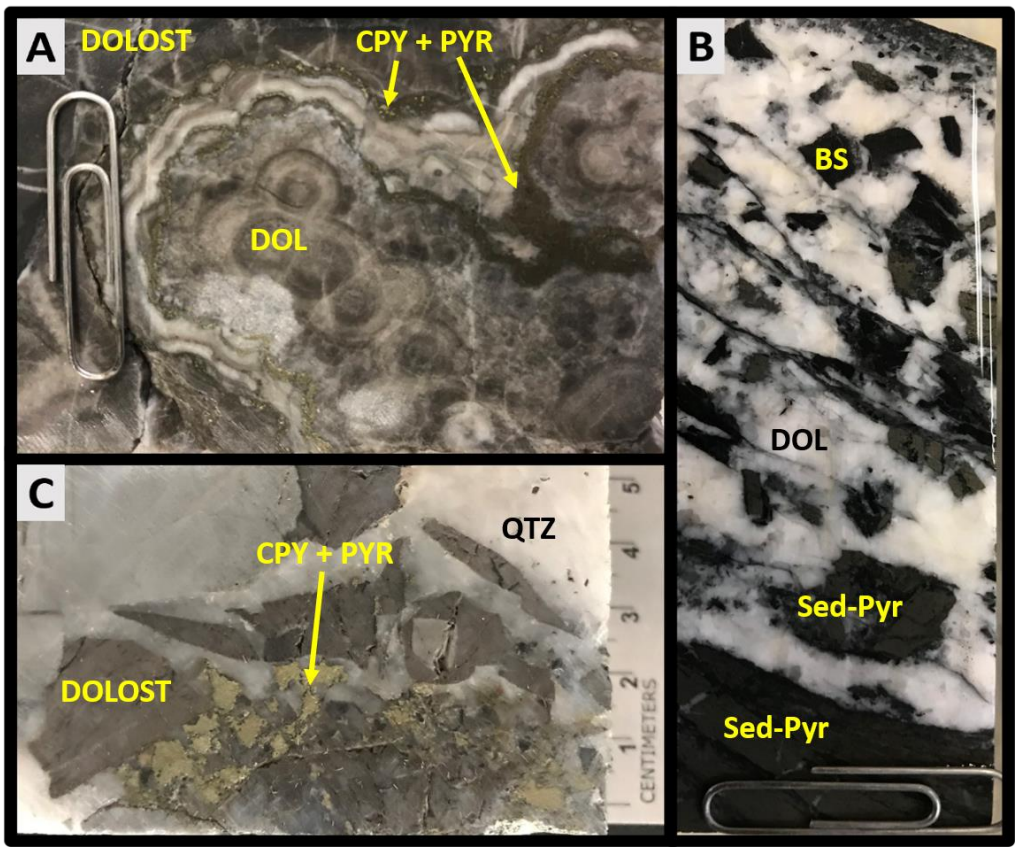

Figure 11: Lowry gangue textures- A- SC12-168-351.96: crustiform dolomite rimmed by pyrite and chalcopyrite; B- SC21-263-260.32: dolomite dissolution breccia- white sparry dolomite with clasts of black shale and sedimentary pyrite; C- SC12-160-415.15: brecciated and silicified dolomitic (?) shale in quartz with pyrite and chalcopyrite. Bs- black shale, cpy- chalcopyrite, dol- dolomite, dolost- dolostone, sed-pyr- sedimentary pyrite, pyr- pyrite, qtz- quartz.

Bitumen often occurs within the coarse dolomite cores, with textures often resembling drops of hydrocarbons under reflected light (Figure 13 B), signifying that bitumen originated as liquid hydrocarbon rather than solid kerogen. Bitumen also occurs as stringers and masses in cross-cutting veins (Figure 12 D, Appendix B), further evidence that it was transported, as a liquid. The bitumen is believed to be a result of maturation of carbonaceous material from the Newland shale and dolostone beds. Dissolution breccias commonly occur as sparry white dolomite with angular clasts of sedimentary pyrite and/or black shale (Figure 11, B). Mosaic breccias, consisting of fine-grained, recrystallized dolostone cut by thin white hydrothermal dolomite veins +/- sulfides are also common.

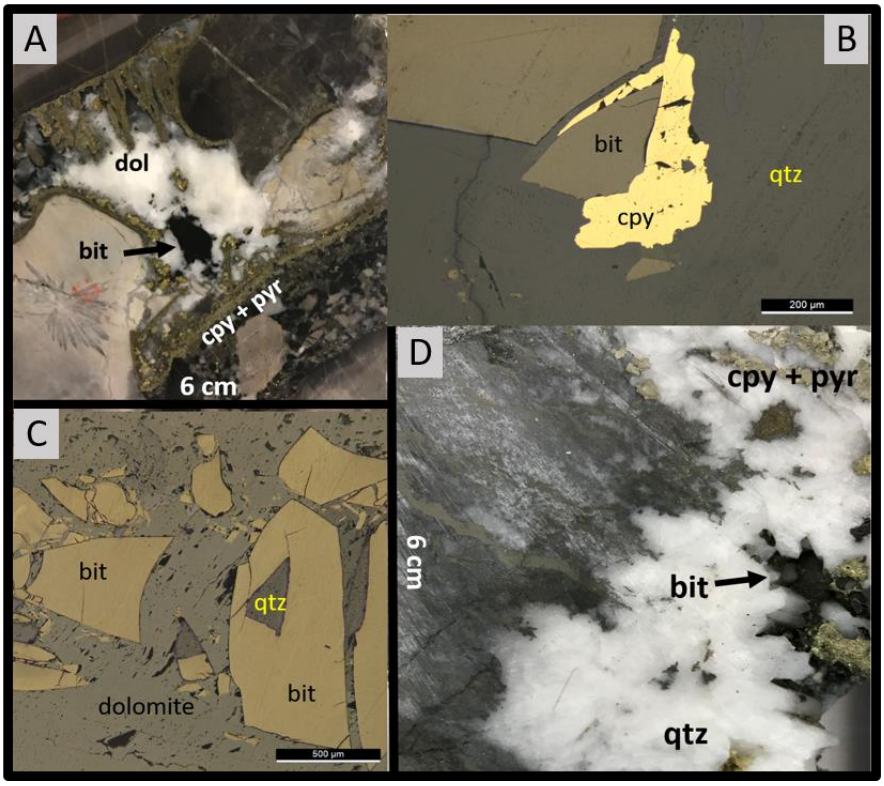

Figure 12: Lowry solid bitumen textures with gangue and sulfide. A, B, C- SC12-160-395.62: coarse bitumen coring sparry dolomite with pyrite and chalcopyrite replacing debris flow matrix; B: photomicrograph of fractured bitumen in quartz partially engulfed by chalcopyrite; C: photomicrograph of bitumen with quartz in sparry dolomite; D: SC12-163-498.85: silicified pyrite tubes cut by quartz vein with bitumen, chalcopyrite and pyrite. Bitumen and chalcopyrite are filling a vug in the quartz vein. Bit- bitumen, cpy- chalcopyrite, dol- dolomite, qtz- quartz

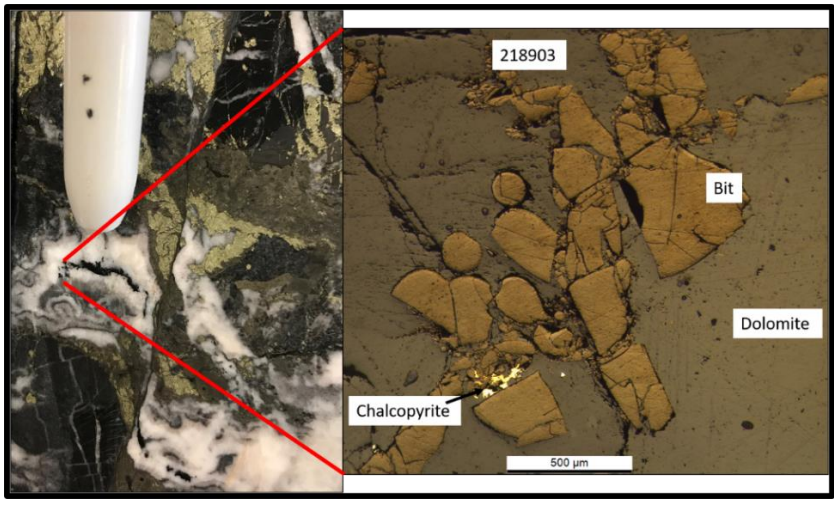

Figure 13: SC12-168-349.98: Hand sample and photomicrograph of solid bitumen with dolomite and chalcopyrite. The mean T_{peak} of this sample (218903) was 236.1°C (Table 16).

Anhydrite was observed in one drill hole cutting the Chamberlain Fm. (Yc) approximately 15m below the Ynl-Yc contact (Figure 14). Multiple occurrences of similar purple anhydrite veins have been observed in drill core through the lower Newland Fm. at Lowry (Zieg, G.A., personal communication, September 2021).

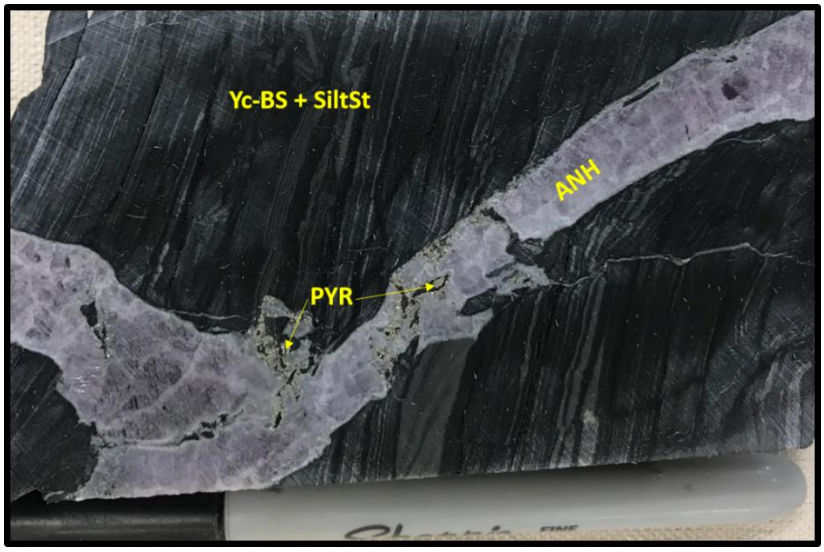

Figure 14: SC21-263-529.13: Anhydrite-pyrite vein cutting shale (black) and silt (grey) of Yc.

3.2. Stable Isotopes

3.2.1. Sulfur Isotopes

Chalcopyrite (n=13) and pyrite (n=1) separates from the Lowry Middle (n=11) and Lower (n=3) sulfide zones were analyzed for $\delta^{34}S$, as was one separate from an anhydrite vein cutting the Chamberlain Fm. Samples were collected from chalcopyrite in veins and replacement or engulfing textures of pyrite and dolomite in the Lowry MSZ and LSZ. The $\delta^{34}S$ values of chalcopyrite and pyrite separates ranged from -3.6 to + 3.4 ‰, with a mean of -0.4 ‰ (n=14), and the anhydrite vein cutting Yc had a value of 17.3‰ (Table 3).

Table 3: $\delta^{34}S$ results and sample descriptions. Depths are reported in meters from the top of angled drill holes and do not represent absolute depth from the surface. Bit- bitumen, bs- black shale, cpy- chalcopyrite, dfc- debris flow conglomerate, dol- dolomite, pyr- pyrite, qtz- quartz

Sample ID	$\delta^{34}S$ VCDT	Mineral	Drill Hole	Drill Depth (meters)	Zone	Lith	Sample Description
218915	2.5	Chalcopyrite	SC12-163	457.00	top of MSZ	Ynl	Cpy from 2-4cm vein with pyr and dol cutting pyr mud and bs
218916	2.2	Chalcopyrite	SC12-163	481.65	MSZ	Ynl	Cpy from 2-4cm vein with pyr cutting and replacing dfc
223504	-3.6	Chalcopyrite	SC12-160	415.40	MSZ	Ynl	Cpy with pyr and dol in silicified dfc
223505	-0.9	Chalcopyrite	SC12-160	415.15	MSZ	Ynl	Cpy with qtz and pyr in qtz dolostone/shale breccia
223506	-1.4	Chalcopyrite	SC12-160	414.30	MSZ	Ynl	Cpy from 1-3 cm thick, 60 cm long vein with pyr cutting dolomite in silicified large clast dolostone/shale dissolution breccia
223512	-2.1	Chalcopyrite	SC12-154	374.70	MSZ	Ynl	Cpy replacing matrix with pyr and dol in dolostone and shale mosaic breccia
223514	2.9	Chalcopyrite	SC12-154	380.30	MSZ	Ynl	Cpy replacing matrix with pyr and dol in dolostone and shale mosaic breccia
223519	-2.2	Chalcopyrite	SC12-154	406.92	MSZ	Ynl	Cpy with sparry-white dol, pyr and qtz replacing net-texture pyrite
223522	3.4	Chalcopyrite	SC12-157	408.38	MSZ	Ynl	Cpy with sparry-white dol replacing breccia matrix
223524	-1.9	Chalcopyrite	SC12-157	416.72	MSZ	Ynl	Cpy from 1-3.5 cm vein with pyr curring bs and pyr mud
223526	-0.5	Chalcopyrite	SC12-157	423.40	MSZ	Ynl	Cpy from 1.5-2.5 cm vein with pyr cutting pyr mud and net texture
223532	-0.2	Chalcopyrite	SC21-263	501.65	below LSZ	Ynl	Cpy from bleb in banded shale/dolostone with soft sed deformation
223532	-0.4	Pyrite	SC21-263	501.65	below LSZ	Ynl	Pyr from bleb in banded shale/dolostone with soft sed deformation
223542	-2.7	Chalcopyrite	SC21-256	798.95	LSZ	Ynl	Cpy from 2.5-3 cm thick vein w/pyr, ten
223530	17.3	Anhydrite	SC21-263	529.13	-	Yc	Sample from 1 cm thick purple anhydrite vein cutting black siltstone

3.2.2. Carbon and Oxygen Isotopes of Carbonates

Carbonate gangue (n = 25) and one Newland Fm. dolomitic shale from the Lowry MSZ and LSZ, and Johnny Lee USZ and LSZ were analyzed for $\delta^{13}C$ and $\delta^{18}O$. Separates were

collected from dolomite gangue from veins, breccias and replacement textures described in section 4.1. $\delta^{13}C$ and $\delta^{18}O$ of dolomite from the Lowry MSZ and LSZ (n= 19) ranged from -4.8 to 0.7‰, with a mean of -2.1 ‰. and 18.7 to 22.2 ‰ with a mean of 20.6‰ respectively. $\delta^{13}C$ and $\delta^{18}O$ of dolomite rhombs from the Johnny Lee USZ and LSZ (n=4) ranged from -5.2 to -4.2‰, with a mean of -4.6‰ and 22.1 to 19.0‰ with a mean of 19.7‰ respectively. $\delta^{13}C$ and $\delta^{18}O$ of lower Newland Fm. dolomitic shale from the Johnny Lee USZ (Bbutte-4, n=1) were -0.8‰ and 22.1‰ respectively. $\delta^{13}C$ and $\delta^{18}O$ of strontianite from the Johnny Lee USZ (n=2) ranged from -12.8‰ to -18.9‰ and 17.6‰ to 18.0‰ with a mean of -15.8‰ and 17.8‰ respectively (Table 4). See section in Appendix A for more details on the Sr-rich samples.

Table 4: $\delta^{13}C$ and $\delta^{18}O$ of carbonates results and sample descriptions. Depths are reported in meters from the top of angled drill holes, and do not represent absolute depth from surface. Bit- bitumen, cpy- chalcopyrite, dol- dolomite, pyr- pyrite, qtz- quartz, stron- strontianite. * Samples were collected in 2012 and analyzed following the method described in section 3.3.3.

Sample ID	$\delta^{13}C$ vs. VPDB	$\delta^{18}O$ vs. VSMOW	Drill Hole	Drill Depth (meters)	Zone	Material	Sample Description
223528	-0.6	20.3	SC21-263	260.32	MSZ	Dol	Sparry-white dol replacing breccia matrix
218905	-0.6	19.9	SC12-168	351.42	MSZ	Dol	Sparry white crustiform dol in dissolution breccia
218905B	-1.2	19.5	SC12-168	351.42	MSZ	Dol	Sparry white-grey crustiform dol rimming sparry white dol in dissolution breccia
223523	-0.8	20.6	SC12-157	410.42	MSZ	Dol	Sparry white-grey dol w/cpy cutting and replacing debris flow and net-textured pyr
223529	-1.0	20.5	SC21-263	272.26	MSZ	Dol	Sparry-white dol with bit, pyr and cpy from dolostone dissolution
223522	-1.4	21.2	SC12-157	408.38	MSZ	Dol	Sparry-white dol with cpy replacing breccia matrix
218904	-1.4	20.5	SC12-168	351.22	MSZ	Dol	Sparry-white-crustiform dol from dolostone dissolution breccia (?) with cpy, pyr and minor bitumen.
223525	-1.5	21.5	SC12-157	419.24	MSZ	Dol	Sparry-white dol from vein w/bitumen

218903	-1.6	20.1	SC12-168	349.98	MSZ	Dol	Sparry-white-crustiform dol with bit, pyr and cpy along structure
223519	-1.6	20.6	SC12-154	406.92	MSZ	Dol	Sparry-white dol with cpy, pyr and qtz replacing net-texture pyrite
223509	-2.9	19.8	SC12-160	367.89	MSZ	Dol	Sparry-white-ferroan dol that oxidizes on weathered surfaces
223507	-3.1	20.8	SC12-160	395.62	MSZ	Dol	Sparry-white dol with bit, pyr and cpy replacing dfc matrix
218919	0.7	21.8	SC12-163	651.66	LSZ	Dol	Sparry white dol from qtz-dol-pyr-bit replacement of net-texture pyrite matrix.
218918	-3.1	19.3	SC12-163	650.6	LSZ	Dol	Dol dolostone with soft sediment deformation around rhomb, appears autochthonous
223535	-3.2	21.6	SC21-263	482.19	LSZ	Dol	Sparry white-grey dolomite in dissolution texture
223539	-3.6	20.2	SC21-256	784.66	LSZ	Dol	Sparry-white dol, from dissolution breccia, with cpy
223533.1	-4.1	22.2	SC21-263	502.79	LSZ	Dol	Dolostone from grey clast or host rock cut by vein
223534	-4.1	18.7	SC21-263	481.13	LSZ	Dol	Dol from porphyroblast in silt shale with calcite filled molar tooth structures around porphyroblasts
223533	-4.8	21.9	SC21-263	502.79	LSZ	Dol	Sparry-white dol with pyr and cpy in vein cutting dolostone
*Bbutte-5	-5.2	19.0	SC11-048	358.84	LSZ	Dol	White sparry dol megacryst
*Bbutte-6	-4.5	20.2	SC11-29	429.9	LSZ	Dol	White sparry dol megacryst
*Bbutte-7	-4.2	19.5	SC11-048	356.9	LSZ	Dol	White sparry dol megacryst
*Bbutte-8	-4.5	20.3	SC12-100	412.3	LSZ	Dol	White sparry dol megacryst
*Bbutte-4	-0.8	22.1	SC11-016	184	USZ	Dolomitic Shale	Dolomite rich Newland Fm.
*Bbutte-1	-12.8	17.6	SC12-120	146	USZ	Stron	Footwall sample rich in stron and celestine, as well as bornite and chalcocite
*Bbutte-2	-18.9	18.0	SC12-120	146.3	USZ	Stron	Footwall sample rich in stron and celestine, as well as bornite and chalcocite

3.2.3. Carbon of Bitumen

Three separates of bitumen from the Lowry MSZ were analyzed for $\delta^{13}C$. Separates were collected from dolomite or quartz veins or replacement gangue with chalcopyrite +/- pyrite and tennantite. Lowry $\delta^{13}C$ of bitumen ranged from -30.4 to -33.5‰ with a mean of 31.5‰ (n=3) (Table 5).

Table 5: C isotopes of solid bitumen and sample descriptions from this study. Depths are reported in meters from the top of angled drill holes, and do not represent absolute depth from surface. Bit- bitumen, cpy- chalcopyrite, dfc- debris flow conglomerate, dol- dolomite, pyr- pyrite, qtz- quartz.

Sample ID	$\delta^{13}C$ vs. VPDB	Drill Hole	Drill Depth (meters)	Zone	Sample Description
223525	-30.4	SC12-157	419.24	MSZ	Bit from sparry-white dol vein
223507b	-30.7	SC12-160	395.62	MSZ	Bit with sparry-white dol, pyr and cpy replacing dfc matrix
218917	-33.5	SC12-163	498.85	MSZ	Bit with cpy and pyr in qtz vein cutting silicified net-texture pyr

3.2.4. Oxygen of Quartz

Six separates of quartz from the Lowry USZ and MSZ were analyzed for $\delta^{18}O$. Separates were collected from quartz veins containing chalcopyrite +/- tennantite, pyrite and bitumen. Lowry $\delta^{18}O$ of quartz ranged from 21.0 to 22.8‰ with a mean of 21.9‰ (n=6) (Table 6).

Table 6: O isotopes of quartz and sample descriptions from this study. All samples are from the lower Newland Fm. in the Lowry deposit. Depths are reported in meters from the top of angled drill holes, and do not represent absolute depth from surface. Bs- black shale, cpy- chalcopyrite, pyr- pyrite, qtz- quartz.

Sample ID	$\delta^{18}O$ vs VSMOW	Drill Hole	Drill Depth (meters)	Zone	Sample Description
218909	21.0	SC12-168	230.52	USZ	Qtz with cpy and bit in vein cutting silicified net-texture pyr
218911	22.7	SC12-168	237.19	USZ	Qtz with cpy and bit in vein cutting silicified net-texture pyr

218913	21.9	SC12-168	241.28	USZ	Vuggy qtz with cpy and bit in vein cutting silicified shale with pyr
223505	21.2	SC12-160	415.15	MSZ	Qtz with cpy and pyr in silicified qtz dolostone/shale breccia
223515	21.9	SC12-154	385.77	MSZ	Qtz with cpy and pyr in/around pyr mud and bs
223516	22.8	SC12-154	383.83	MSZ	Qtz with cpy and pyr in silicified qtz dolostone/shale breccia

3.3. Radiogenic Isotopes

3.3.1. Pb Isotopes

The isotopes of Pb are reported as the ratios $^{206}Pb/^{204}Pb$, $^{207}Pb/^{204}Pb$, $^{208}Pb/^{204}Pb$, which were derived from the raw values of each isotope measured by the method described in section 3.4. All Pb isotope results from mineral separates are reported in Table 7. Ratios in chalcopyrite (n=5) ranged from 17.182 – 17.380, 15.548 – 15.616 and 36.957 – 37.222 for $^{206}Pb/^{204}Pb$, $^{207}Pb/^{204}Pb$, $^{208}Pb/^{204}Pb$ respectively. Ratios in dolomite (n=4) ranged from 17.763 – 18.347, 15.577 – 15.620, 37.464 – 38.086 for $^{206}Pb/^{204}Pb$, $^{207}Pb/^{204}Pb$, $^{208}Pb/^{204}Pb$ respectively. Values from one anhydrite sample were 18.249, 15.630 and 38.094 for $^{206}Pb/^{204}Pb$, $^{207}Pb/^{204}Pb$, $^{208}Pb/^{204}Pb$ respectively.

Table 7: Pb isotopes of mineral separates and sample descriptions from this study. Depths are reported in meters from the top of angled drill holes, and do not represent absolute depth from surface. Cpy- chalcopyrite, dfc- debris flow conglomerate, pyr- pyrite, qtz- quartz, ten- tennantite; Ynl- lower Newland Fm., Yc- Chamberlain Fm.

Sample ID	$^{208}Pb/^{204}Pb$	$^{207}Pb/^{204}Pb$	$^{206}Pb/^{204}Pb$	Mineral	Drill Hole	Drill Depth (meters)	Zone	Lith	Sample Description
223506	37.201	15.596	17.380	Chalcopyrite	SC12-160	414.30	MSZ	Ynl	Cpy from 1-3 cm thick, 60 cm long vein with pyr cutting dolomite in silicified large clast dolostone/shale dissolution breccia
223512	37.056	15.606	17.330	Chalcopyrite	SC12-154	374.70	MSZ	Ynl	Cpy replacing matrix with pyr and dol in dolostone and

									shale mosaic breccia
223526	36.957	15.616	17.182	Chalcopyrite	SC12-157	423.40	MSZ	Ynl	Cpy from 1.5-2.5 cm vein with pyr cutting pyr mud and net texture
218916	37.010	15.572	17.199	Chalcopyrite	SC12-163	481.65	MSZ	Ynl	Cpy from 2-4cm vein with pyr cutting and replacing dfc
223542	37.222	15.548	17.184	Chalcopyrite	SC21-256	798.95	LSZ	Ynl	Cpy from 2.5-3 cm thick vein w/pyr, ten
218905	37.958	15.577	18.291	Dolomite	SC12-168	351.42	MSZ	Ynl	Sparry white crustiform dol in dissolution breccia
218905b	37.464	15.616	17.763	Dolomite	SC12-168	351.42	MSZ	Ynl	Sparry white-grey crustiform dol rimming sparry white dol in dissolution breccia
223522	37.966	15.597	18.218	Dolomite	SC12-157	408.38	MSZ	Ynl	Sparry-white dol with cpy replacing breccia matrix
223539	38.086	15.620	18.347	Dolomite	SC21-256	784.66	LSZ	Ynl	Sparry-white dol, from dissolution breccia, with cpy
223530	38.094	15.630	18.249	Anhydrite	SC21-263	529.13	-	Yc	Anhydrite from 1-3 cm violet vein cutting Yc

All Pb isotope results from bulk-rock samples are reported in Table 8. Ratios from the Neihart Fm. sandstone and quartzite (n=5) ranged from 20.993 - 44.376, 15.914 - 18.509, 39.039 - 78.792 for $^{206}Pb/^{204}Pb$, $^{207}Pb/^{204}Pb$, $^{208}Pb/^{204}Pb$ respectively. Ratios from the Chamberlain Fm. siltstone had values of 27.393, 16.576 and 46.375 for $^{206}Pb/^{204}Pb$, $^{207}Pb/^{204}Pb$, $^{208}Pb/^{204}Pb$ respectively.

Table 8: Pb isotopes of bulk rock samples and sample descriptions from this study. Depths are reported in meters from the top of angled drill holes, and do not represent absolute depth from surface. Bn- bornite, cpy- chalcopyrite, pyr- pyrite, qtz- quartz; Yc- Chamberlain Fm., Yne- Neihart Fm.

Sample ID	$^{208}Pb/^{204}Pb$	$^{207}Pb/^{204}Pb$	$^{206}Pb/^{204}Pb$	Material	Drill Hole	Drill Depth (meters)	Lith	Sample Description
218907	46.375	16.576	27.393	Siltstone	SC21-257	904.95	Yc	alternating black wavy-bedded silt with grey silt
223537	54.315	17.416	35.727	Quartzite	SC21-263	739.53	Yne	white and maroon-red quartzite with very thin laminae of bright red hematite
223546	39.039	15.914	20.993	Quartzite	SC21-261	524.45	Yne	fine grained quartzite with blotchy hematite throughout; hematite and Cu-ox staining on fracture faces
223550	61.439	18.358	41.414	Sandstone	SC21-261	594.06	Yne	Conglomeratic unit with sub-rounded red-blue-grey chert and qtz pebbles interbedded with sand; pyr in sand and conglomerate along planes about 20° off of bedding. Pyr is brassy diagenetic, not sedimentary
223547	54.196	17.312	31.802	Sandstone/quartz-sand pebble conglomerate	SC21-261	565.83	Yne	Representative sample of sandstone (grains not fused) with silty interbeds
223549	78.792	18.509	44.376	Quartz sand-pebble conglomerate	SC21-261	570.80	Yne	Conglomeratic unit w/red-blue-grey chert and qtz sub-rounded pebbles with interbeds of sand; 0.5-2mm crystals of bn, cpy and pyr in conglomerate

3.3.2. Sr Isotopes

The isotopes of Sr are reported as the ratios $^{87}Sr/^{86}Sr$, which were derived from the raw values of each isotope measured by the method described in section 3.4. $^{87}Sr/^{86}Sr$ of Lowry MSZ and LSZ dolomite (n=4) ranged from 0.7057 to 0.7072 with a mean of 0.7065. $^{87}Sr/^{86}Sr$ of strontianite, barite and dolomite from the Johnny Lee USZ and LSZ (n=5) ranged from 0.7047 to 0.7064 with a mean of 0.7052 (Table 9). A broad range of $^{87}Sr/^{86}Sr$ was measured in Lower Belt lithologies from the BBCP ranging from 0.7053 in the lower Newland at the Johnny Lee USZ to 0.8936 in the Chamberlain siltstone (Table 10).

Total Sr and Rb concentrations from the bulk-rock samples are reported in Table 11. Total Rb concentration in bulk rock samples was found to be low, and therefore, no attempt was made in this study to correct the Sr-isotope values for ^{87}Rb decay.

Table 9: Sr isotopes of mineral separates and sample descriptions from this study. Depths are reported in meters from the top of angled drill holes, and do not represent absolute depth from surface. Cpy- chalcopyrite, dol- dolomite, pyr- pyrite, qtz- quartz; stron = strontianite; bar = barite; Ynl- lower Newland Fm. * Johnny Lee USZ and LSZ samples collected and analyzed in August 2012.

Sample ID	$^{87}Sr/^{86}Sr$	Mineral	Drill Hole	Drill Depth (meters)	Zone	Lith	Sample Description
218905	0.7065	Dolomite	SC12-168	351.42	Lowry MSZ	Ynl	Sparry white crustiform dol in dissolution breccia
218905b	0.7067	Dolomite	SC12-168	351.42	Lowry MSZ	Ynl	Sparry white-grey crustiform dol rimming sparry white dol in dissolution breccia
223522	0.7057	Dolomite	SC12-157	408.38	Lowry MSZ	Ynl	Sparry-white dol with cpy replacing breccia matrix
223539	0.7072	Dolomite	SC21-256	784.66	Lowry LSZ	Ynl	Sparry-white dol, from dissolution breccia, with cpy
223530	0.7071	Anhydrite	SC21-263	529.13	-	Yc	anhydrite from 1-3 cm violet vein cutting Yc
*Bbutte-1	0.7047	Strontianite	SC12-120	146	Johnny Lee USZ	Ynl	Stron with celestine
*Bbutte-2	0.7047	Strontianite	SC12-120	146.3	Johnny Lee USZ	Ynl	Stron with celestine, pyr and cpy
*Bbutte-3	0.7048	Barite	SC11-016	221	Johnny Lee USZ	Ynl	Feathery bar
*Bbutte-7	0.7064	Dolomite	SC11-048	356.9	Johnny Lee LSZ	Ynl	White sparry dol megacryst with pyr and cpy
*Bbutte-8	0.7052	Dolomite	SC12-100	412.3	Johnny Lee LSZ	Ynl	White sparry dol megacryst with pyr and cpy

Table 10: Sr isotopes of bulk rock samples and sample descriptions from this study. Depths are reported in meters from the top of angled drill holes, and do not represent absolute depth from surface. Bn- bornite, cpy- chalcopyrite, pyr- pyrite, qtz- quartz; Ynl- lower Newland Fm., Yc- Chamberlain Fm., Yne- Neihart Fm.

Sample ID	$^{87}Sr/^{86}Sr$	Rock Type	Hole_ID	Depth (meters)	Lith	Sample Description
218907	0.8936	Siltstone	SC21-257	904.95	Yc	alternating black wavy-bedded silt with grey silt
223537	0.7587	Quartzite	SC21-263	739.53	Yne	white and maroon-red quartzite with very thin laminae of bright red hematite
223546	0.7186	Quartzite	SC21-261	524.45	Yne	fine grained quartzite with blotchy hematite throughout; hematite and Cu-ox staining on fracture faces
223550	0.7334	Sandstone	SC21-261	594.06	Yne	Conglomeratic unit with sub-rounded red-blue-grey chert and qtz pebbles interbeded with sand; pyr in sand and conglomerate along planes about 20° off of bedding. Pyr is brassy diagenetic, not sedimentary
223547	0.7472	Sandstone/quartz sand pebble conglomerate	SC21-261	565.83	Yne	representative sample of sandstone (grains not fused) with silty interbeds
223549	0.7201	Quartz sand-pebble conglomerate	SC21-261	570.80	Yne	conglomeratic unit w/red-blue-grey chert and qtz sub-rounded pebbles with interbeds of sand; 0.5-2mm crystals of bn, cpy and pyr in conglomerate
223548	0.8262	Siltstone	SC21-261	564.00	Yne	silt bed 90m below Yc contact
*Bbutte-4	0.7053	Dolomitic Shale	SC11-016	184	Ynl	parallel laminated dolomitic shale from JL USZ

Table 11: Total Rb and Sr content from ICP-MS analysis of bulk-rock samples from the Lowry deposit. Depths are reported in meters from the top of angled drill holes, and do not represent absolute depth from surface. Sample descriptions correlate to samples in Table 10. Yc- Chamberlain Fm., Yne- Neihart Fm.

Sample ID	Rb (ppm)	Sr (ppm)	Rb/Sr (by ICPMS)	Rock Type	Drill Hole	Depth (meters)	Lith
218907	90.5	24.9	3.64	Siltstone	SC21-257	904.95	Yc
223537	21.6	24.7	0.87	Quartzite	SC21-263	739.53	Yne
223546	2.15	19.4	0.11	Quartzite	SC21-261	524.45	Yne
223550	6.10	18.3	0.33	Sandstone	SC21-261	594.06	Yne
223547	8.30	14.0	0.59	Sandstone/quartz sand pebble conglomerate	SC21-261	565.83	Yne
223549	3.84	40.0	0.10	Quartz sand-pebble conglomerate	SC21-261	570.80	Yne
223548	161	86.9	1.86	Siltstone	SC21-261	564.00	Yne

3.4. Bitumen Reflectance and Temperature Estimates

For this study, reflectance of solid bitumen from the Lowry was measured at the USGS OPL in Reston, VA. The reflectance values measured there were used to calculate peak temperature estimates (Table 12) following Barker and Bone (1995), shown in Equation 1. Mean peak temperature estimated from bitumen reflectance was 223± 8°C (n=8).

$$T_{peak} = (BR_o + 0.9787)/0.0202 \quad (1)$$

Discrepancies were observed between temperature estimates made from different bitumen grains in multiple plugs from single samples. For example, samples 223507 and 223507b are bitumen grains from core sample SC12-160-395.62 and formed under 1 cm apart, but the peak temperature estimates from mean reflectance values for the pair is 5°C apart. This level of difference is in strong agreement with the standard deviation calculated from the mean

temperature estimate for each sample (Table 12). Examples of bitumen used for reflectance analysis are provided in Appendix B.

Table 12: Reflectance values and temperature estimates from Lowry deposit bitumen. Error is a standard deviation; depths are reported in meters from the top of angled drill holes, and do not represent absolute depth from surface. Bit- bitumen, cpy- chalcopyrite, dfc- debris flow conglomerate, dol- dolomite, pyr- pyrite, qtz- quartz.

Sample	BR_o (%)	+/- %	Mean T_{peak} (°C)	+/- °C	Drill Hole	Depth (meters)	Zone	Sample Description
223507	3.3	0.1	212.8	7.1	SC12-160	395.62	MSZ	Bit with sparry-white dol, pyr and cpy replacing dfc matrix
223529	3.3	0.1	213.8	6.6	SC21-263	272.26	MSZ	Bit with sparry white dol, pyr and cpy from dolostone dissolution
218919	3.4	0.1	215.3	6.5	SC12-163	651.66	LSZ	Bit from qtz-dol-pyr replacement of net-texture pyrite matrix.
223507b	3.4	0.1	218.3	7.3	SC12-160	395.62	MSZ	Bit with sparry-white dol, pyr and cpy replacing dfc matrix
223525a	3.4	0.2	218.7	8.1	SC12-157	419.24	MSZ	Bit from sparry white dol vein with pyr
218917	3.6	0.2	228.2	11.4	SC12-163	498.85	MSZ	Bit from milky white qtz vein with pyr and cpy cutting net texture pyr
218903	3.8	0.2	236.1	8.4	SC12-168	349.98	MSZ	Bit with sparry-white-crustiform dol, pyr and cpy along structure
223525b	3.9	0.2	239.5	8.9	SC12-157	419.24	MSZ	Bit from sparry white dol vein with pyr

3.5. Raman Spectroscopy of Carbonaceous Material

Mean peak temperature calculated from Raman spectra of Lowry bitumen was 247 ± 40°C (n=7). Error is reported as a propagated two standard error. As a subset of the bitumen reflectance samples from the Lowry MSZ (n=6) and LSZ (n=1), the peak temperature calculations from Raman analysis are 24°C higher on average than bitumen reflectance.

Table 13: Raman temperature calculations from Lowry deposit bitumen. Error is reported as a propagated two standard error; depths are reported in meters from the top of angled drill holes, and do not represent absolute depth from surface. Bit- bitumen, cpy- chalcopyrite, dfc- debris flow conglomerate, dol- dolomite, pyr- pyrite, qtz- quartz.

Sample	Mean T_{peak} (°C)	°C +/-	n	Drill Hole	Depth (meters)	Zone	Sample Description
223507	262	24	18	SC12-160	395.62	MSZ	Bit with sparry-white dol, pyr and cpy replacing dfc matrix
223507b	264	23	19	SC12-160	395.62	MSZ	Bit with sparry-white dol, pyr and cpy replacing dfc matrix
223525b	265	22	21	SC12-157	419.24	MSZ	Bit from sparry white dol vein with pyr
223529	239	29	12	SC21-263	272.26	MSZ	Bit with sparry white dol, pyr and cpy from dolostone dissolution
218903	240	24	18	SC12-168	349.98	MSZ	Bit with sparry-white-crustiform dol, pyr and cpy along structure
218917	243	23	19	SC12-163	498.85	MSZ	Bit from milky white qtz vein with pyr and cpy cutting net texture pyr
218919	219	24	18	SC12-163	651.66	LSZ	Bit from qtz-dol-pyr replacement of net-texture pyrite matrix.

4. Discussion

4.1. Mineralization Textures

The MSZ of the Lowry deposit displays cross cutting sulfide and gangue textures distinct from the Johnny Lee deposit, where lateral replacement of sedimentary pyrite and debris flow matrix is the typical style of mineralization (Zieg and Lietch, 1998; Graham et al., 2012). These epigenetic textures suggest a late ore fluid under increased lithostatic pressure to cause brittle fracturing of the host lower Newland Fm. However, mineralization at the Lowry deposit remains laterally continuous and strata-bound, and grade is zoned relative to Proterozoic, project-scale structures (Zieg et al., 2013), which display no stockwork veining cutting earlier units (Zieg, G.A., personal communication, September 2020). This suggests that the mineralization at the Lowry MSZ and USZ was controlled by variables specific to the units which host them. The amount of veining and open space fill in the Lowry MSZ requires that pressure was great enough to create fracturing along the MSZ units, and that local dissolution occurred, at least partially, prior to base metal precipitation from hydrothermal fluids.

It is likely that the dolomite interbeds in the Newland Formation were originally deposited as calcite and/or aragonite. Dolomitization could have happened during early diagenesis, through reactions with saline groundwater, or during later hydrothermal fluid circulation. When calcite is converted to dolomite on a mole for mole basis, there is an increase in porosity of roughly 13%, due to the negative change in molar volume (Tucker and Wright, 1990). Some calcite could have dissolved without reprecipitation as dolomite, e.g., if the circulating brines were calcite-undersaturated, which would have created more open space. It is also possible that dolomitization happened during circulation of hydrothermal fluids. However, if the latter was the main process, then one would expect dolomitization to be localized along the

same mineralized structures that host chalcopyrite mineralization. In the case of the Newland Formation, all of the sedimentary carbonate has been dolomitized.

Once zones of open space were created, liquid petroleum formed locally by maturation of organic matter in the Newland Fm. could have migrated into the high-porosity zones. This petroleum was eventually converted into insoluble solid bitumen by one of two mechanisms: 1) thermal chemical alteration (TCA); or 2) thermochemical sulfate reduction (TSR). Kelemen et al. (2008) defined TCA bitumen as forming through low-temperature alteration of petroleum compounds through multiple mechanisms including biodegradation and asphaltene production, while TSR bitumen forms from an abiotic redox reaction that occurs when sulfate oxidizes petroleum to CO_2. TSR is associated with the production of large quantities of H_2S through the reduction of sulfate (Kelemen et al., 2008 and references therein). The two types of solid bitumen can be distinguished by their aromaticity and nitrogen/sulfur ratios (Landis and Castaño, 1995), as well as their reflectance (Machel et al., 1995). These characteristics become increasingly unreliable for distinguishing TCA from TSR as thermal-maturity increases, and nitrogen/sulfur ratios have been shown to be the only reliable technique to distinguish the mechanism of bitumen formation (Kelemen et al., 2010).

Additionally, Machel et al. (1995) showed that TSR of petroleum can lead not only to the formation of solid bitumen, but also carbonate minerals, including dolomite, strontianite and siderite when the associated cations (Mg, Sr, Fe) are available. While all of these minerals are present at BBCP, bitumen alteration is most strongly associated with dolomite at the Lowry deposit, where sparry dolomite is often cored by bitumen **(**Figure 11 A, 12).

The formation of bitumen through TSR and the associated generation of H_2S would have led to ideal deposition sites for chalcopyrite, and textures observed at the Lowry deposit support

the idea that sulfide deposition is associated with these sites (Figure 10 D, 11 A, 12). An influx of metalliferous hydrothermal fluids would have encountered H_2S in open space, causing the precipitation of chalcopyrite through the following reaction:

$$CuCl_3^{2-} + FeCl_2(aq) + 2H_2S(aq) = CuFeS_2 + 5Cl^- + 3H^+ + \tfrac{1}{2}H_2(g) \quad \textbf{(2)}$$

Protons released from **Equation 2** could have dissolved more dolomite, created new open space and helped to maintain porosity needed for hydrothermal fluid flow:

$$2H^+ + CaMg(CO_3)_2 = Ca^{2+} + Mg^{2+} + 2HCO_3^- \quad \textbf{(3)}$$

Dolomite dissolved by **Equation 3** could have reprecipitated elsewhere as vein fillings cutting black shales, due to a rise in pH.

In their study of the Red Dog deposit in Alaska, Kelley et al. (2004) speculated that methane produced by the thermal breakdown of liquid and/or solid hydrocarbons may have induced fluid overpressures that resulted in fracturing and brecciation of the host rock. These void spaces later became sites for Pb-Zn mineralization. Methane-overpressure zones within organic-rich facies of the Newland Fm. could have played a similar role in formation of vein and breccia-hosted copper mineralization at the Lowry deposit.

4.2. Fluid Temperature

The estimated mean peak temperature experienced by bitumen at the Lowry deposit based on bitumen reflectance geothermometry and RSCM was 223± 8°C (n=8) with a range of 212.8 – 239.5°C and 247± 40°C (n=7) with a range of 219 – 265°C respectively. This overlaps with the upper end of temperatures of 125 to 225°C estimated by White et al. (2014) based on the thermodynamic stability of ore minerals at Black Butte. These results suggest that the Black Butte deposit formed at relatively low temperatures, consistent with other SEDEX and sediment-

hosted stratiform copper deposits world-wide that are believed to have formed by circulating basinal brines.

Saintilan and others (2021) reported un-radiogenic Os values from Black Butte chalcopyrite, which they argued reflects a magmatic Os source. The authors speculated that a buried Mesoproterozoic intrusive body, perhaps akin to the c.a. 1,455 Ma tholeiitic dikes cutting the Archean basement in the Ruby Range and Tobacco Root Mountains near the Perry Line (Wooden et al., 1978), was responsible for an influx of Os and, by inference, other metals, such as Cu, Co, and Ag. Syn-rift magmatism during the opening of the Belt-Purcell Basin equivalent to the 1,469 and 1,457 Ma Moyie sills (Sears et al., 1998) would have created an elevated thermal gradient to drive connate fluid convection. However, the style of mineralization and hydrothermal alteration (including bitumen alteration) at BBCP is incompatible with major involvement of magmatic-hydrothermal fluids. Specifically, two distinct magmatic signatures are lacking at the BBCP: 1) the record of high temperature (300-500°C) hydrothermal fluids associated with copper mineralization in magmatic-hydrothermal deposits, 2) the high temperature alteration associated with magmatic-hydrothermal systems or magmatic-driven convection as in volcanic hosted massive sulfide deposits (VHMS) (Ohmoto, 1996). The bitumen gangue in the Lowry deposit did experience temperatures in the upper temperature regime of a SEDEX system (Emsbo, 2016), but silica and dolomite alteration at BBCP are all within the temperature regime of TSR (Machel, 1995), whereas higher temperature alteration products, e.g., sericite, chlorite, would require a higher temperature, lower pH regime as found in known magmatic-hydrothermal mineral systems.

4.3. Carbon and Oxygen Isotopes

As shown in Figure 15, the sparry, hydrothermal dolomite in the Lowry deposit is depleted in both $\delta^{18}O$ and $\delta^{13}C$ relative to sedimentary dolomite in the Newland Formation. The depletion in $\delta^{18}O$ was likely caused by water-rock interaction at temperatures up to 240°C, as has been modeled for dolomite from the MacArthur River deposit of Australia (Large and others, 2001). Some of the depletion in $\delta^{13}C$ could have been caused by incorporation of inorganic carbon sourced by the breakdown of bitumen, which contains extremely light carbon ($\delta^{13}C$ < -30 ‰). Therefore, incorporation of even a small amount of bitumen-C could have lowered the $\delta^{13}C$ of dissolved inorganic carbon in the hydrothermal fluid.

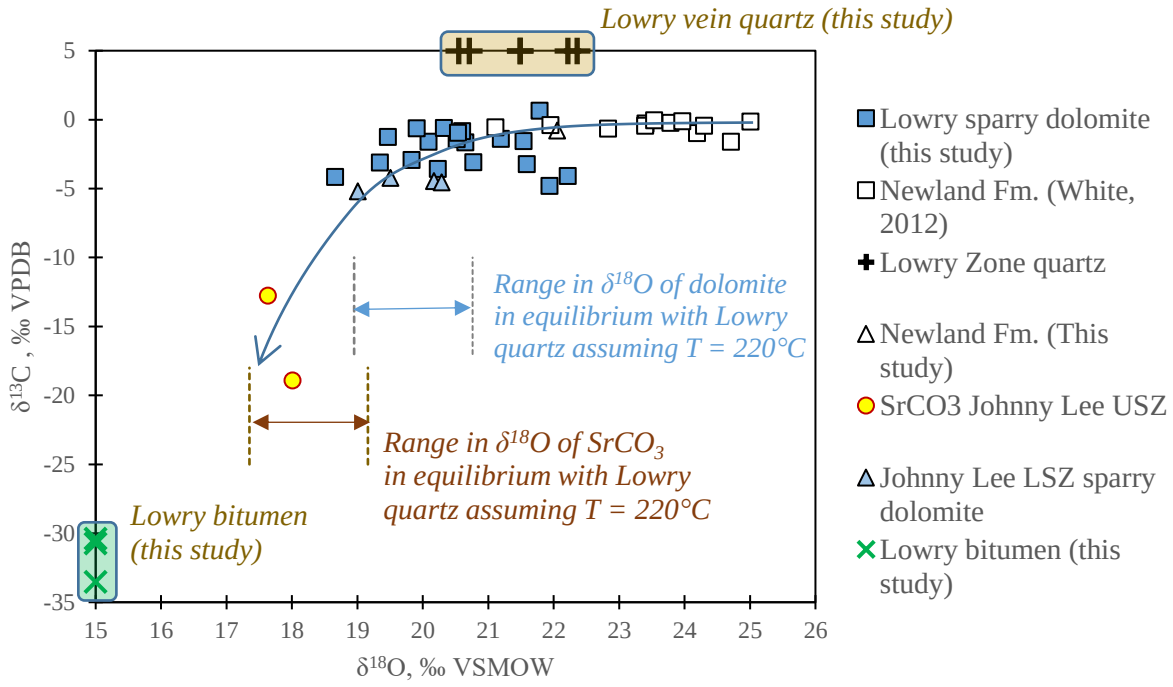

Figure 15: $\delta^{13}C$ and $\delta^{18}O$ values from quartz, dolomite, strontianite ($SrCO_3$) and bitumen from this study, and Newland Fm. from White, 2012. Newland Fm $\delta^{13}C$ and $\delta^{18}O$ reflect seawater carbonate values at the time of deposition. Bracketed blue and brown ranges depict the modeled $\delta^{18}O$ value of dolomite and strontianite forming in equilibrium with Lowry quartz at 220°C.

The $\delta^{18}O$-quartz values reported in Figure 15 are the first published data for hydrothermal quartz from Black Butte. In Figure 15, the equilibrium isotope fractionation equations of Vho et al. (2020) for quartz-dolomite, and quartz-strontianite were used to calculate a range in $\delta^{18}O$ for hydrothermal dolomite and strontianite at a temperature of 220°C, the mean temperature of bitumen from bitumen reflectance analysis inferred here to represent the lower end of ore-forming fluid temperatures at BBCP. At 220°C, quartz is predicted to be about 0.5‰ enriched in $\delta^{18}O$ relative to dolomite and 2.9‰ enriched in $\delta^{18}O$ relative to strontianite (Figure 15) (Vho et al., 2020). The modeled fractionation generally agrees with the results of this study. Whereas hydrothermal quartz from Lowry had an average $\delta^{18}O$ of +21.5‰, hydrothermal dolomite from Lowry has an average $\delta^{18}O$ of +20.6‰, which is 0.9‰ lighter than the quartz, and hydrothermal strontianite from the Johnny Lee had an average $\delta^{18}O$ of +17.8‰, which is 3.6‰ lighter than the quartz.

4.4. Sulfur Isotopes

The S-isotope results presented here are in close agreement with previous studies of the BBCP (Zieg and Lietch, 1998; Lyons et al., 2000; Graham, 2012; Present et al., 2018; Saintilan et al., 2021). Whereas early, sedimentary pyrite of the Newland Formation shows a huge range in $\delta^{34}S$ from -20.2 to +45.2‰ (Present et al., 2018), the $\delta^{34}S$ of epigenetic chalcopyrite in both the Johnny Lee and Lowry deposits is more restricted to values closer to 0‰ (this study, Zieg and Lietch, 1998, Graham, 2012; Present et al., 2018; Saintilan et al., 2021).

Multiple authors have proposed two distinct mechanisms for these ore-stage $\delta^{34}S$ values: 1) a magmatic sulfur source (Zieg and Lietch, 1998; Saintilan et al., 2021) and 2) thermochemical-sulfate-reduction (TSR), by which hydrothermal fluids reduce seawater sulfate to H_2S while oxidizing organic carbon to HCO_3^- (Graham, 2012; Present et al., 2018).

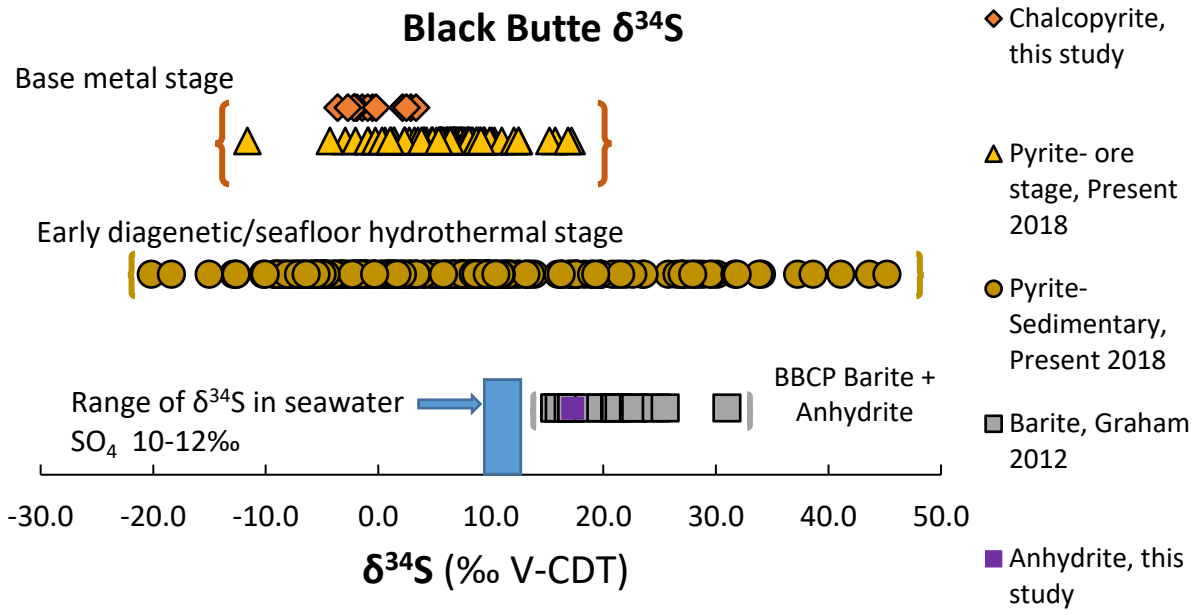

Figure 16: $\delta^{34}S$ values of pyrite, chalcopyrite and barite from BBCP. Pyrite from Present et al., 2018; Barite from Graham, 2012; Chalcopyrite from this study. BSR- huge spread in $\delta^{34}S$ from pyrite textures that reflect early diagenetic conditions (colloform, nodular, mottled) and sulfate reduction by bacteria from a seawater sulfate source. Base metal stage, euhedral-to-irregular coarse pyrite and chalcopyrite with a narrower $\delta^{34}S$ range, likely formed from thermochemical reduction of pore-water sulfate. Bar- barite, cpy- chalcopyrite, pyr- pyrite.

TSR is a mechanism that replaces bacterial sulfate reduction (BSR) at temperatures exceeding 80 - 100°C (Machel et al., 1995, 2001). The process requires sulfate in the dissolved form, either as seawater, porewater, or dissolution of soluble sulfate minerals such as gypsum and anhydrite. Products of TSR include dissolved H_2S, metal-sulfide minerals, carbonate minerals, bitumen (when crude oil is present) and oxidized hydrocarbons (Machel et al., 1995). In sediment-hosted copper deposits, gypsum and/or anhydrite can be important sources of sulfate for TSR (Haynes, 1986; Brown, 1997). The presence of anhydrite in the periphery of the Lowry deposit suggests that it may have been a sulfate source, though little evidence would remain after later dissolution by hot connate brines.

Results from this study suggest that: 1) bacterial sulfate reduction (BSR) was the likely mechanism for precipitation of early sedimentary to diagenetic pyrite, and 2) that sulfur in the Lowry and Johnny Lee deposits has a similar origin, despite differences in the style of mineralization and the different locations of the LSZ, overlying MSZ and USZ on opposite sides of the Volcano Valley reverse fault. Under an increasing thermal regime in the Belt Sea during Newland time, either from increasing burial depths or syn-rift magmatism, TSR would have replaced BSR, producing H_2S, carbonate minerals (sparry dolomite) and bitumen, and creating favorable facies for the precipitation of copper-rich sulfides. While the isotopic fractionation from SO_4^{2-} to S^{2-} attributed to BSR is broad (-15 to - 65‰), fractionation through TSR is relatively narrow (-10‰ at 200°C) (Machel et al., 1995). Hence, the shift from BSR to TSR can explain the shift from broad $\delta^{34}S$ values in pre-copper, sedimentary pyrite, to the narrower range in base-metal stage sulfides (Figure 16). Present et al. (2018) determined that marine sulfate during Newland deposition had a $\delta^{34}S$ value between +10 – 12‰, reduction of which through TSR at 200°C would produce $\delta^{34}S$ values of 0 – 2‰.

Based on the peak temperatures experienced by bitumen at the Lowry deposit, approximately 220 – 250°C, it is thermodynamically unlikely that copper was transported in solution with H_2S. For a copper-rich fluid to coexist with H_2S, fluid temperatures would need to exceed 250-300°C, and pH would need to be at least moderately acidic (Xiao et al., 1998). Copper can be carried in solution at low to moderate (40-300°C) temperatures, and in the absence of H_2S, as cuprous chloride complexes, e.g., $CuCl_2(aq)$ or $CuCl_3^-$ as shown by Rose (1976) and Xiao et al. (1998). Copper transported with chloride, likely sourced from seawater or evaporite minerals, would have precipitated upon encountering H_2S-rich pore space in carbonate interbeds within the Newland Fm.

4.5. Strontium Isotopes

Strontium isotopes have been used as a tool for inferring fluid and metal sources in hydrothermal ore deposits (Kessen et al., 1981; Deng et al., 2015; Movahednia et al., 2020; Maghfouri et al., 2021) and were applied in this study for those purposes. Gangue minerals including calcite, dolomite, strontianite, and barite, incorporate Sr from ore-forming fluids, recording the initial ratio of ore-forming fluids, and potentially a metal source. The radiogenic isotope of rubidium, ^{87}Rb, decays to ^{87}Sr with a half-life of 49.23 Ga, while ^{86}Sr is stable. Because of their low Rb content, incorporation of radiogenic ^{87}Sr in carbonate minerals is negligible and their present-day Sr values should not require correction to estimate initial Sr-isotope ratios (Ruiz et al., 1988 and references therein).

The strontium values shown in Figure 17 display two distinct populations: 1) bulk rock samples from the Neihart and Chamberlain fms. from this study with highly variable $^{87}Sr/^{86}Sr$ values that span from 0.719 to 0.894, and 2) mineral separates of strontianite, barite, dolomite and anhydrite from this study, and bulk rock samples of unaltered dolostone from the Newland Fm. published by Hall and Veizer (1996), with a less radiogenic range of $^{87}Sr/^{86}Sr$ values that span from 0.7047 to 0.7072. Less radiogenic samples of the second population (Figure 17 B) had low initial Rb/Sr and record a range between seawater strontium at the time of mineralization and end member crustal strontium assimilated through fluid interaction with crustal rocks. The much more radiogenic samples of the Neihart and Chamberlain fms. reflect a higher initial Rb/Sr ratio, likely due to Rb-rich terrigenous clastic material.

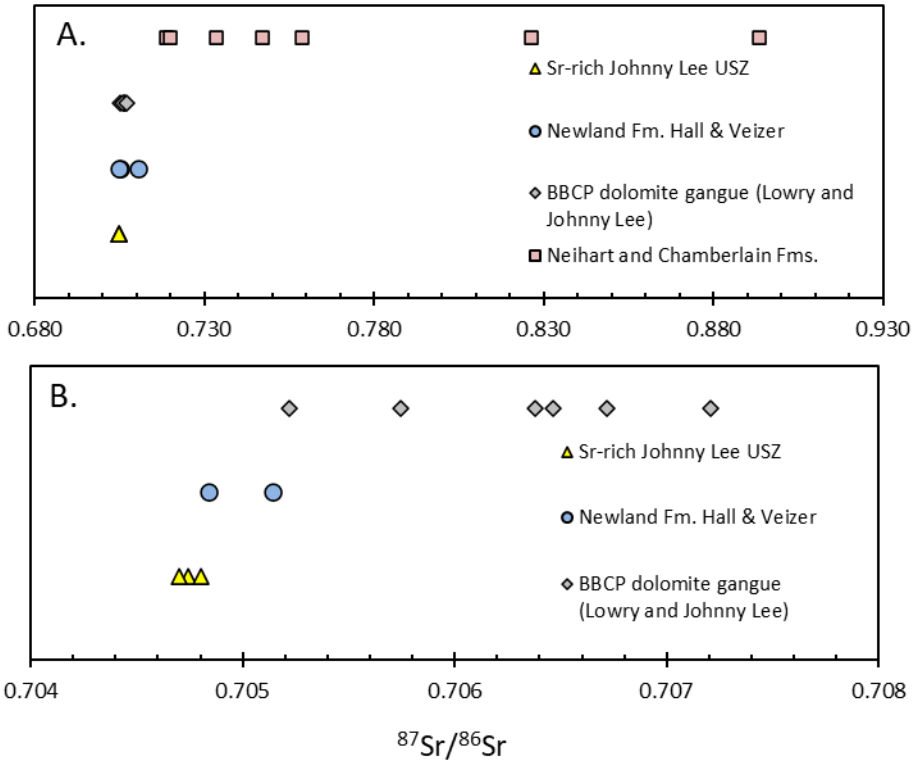

Figure 17: Sr-isotope composition of samples of Newland and Neihart formations. A) All samples; B) Expanded scale to show variations in Newland Fm. carbonate minerals, including Sr-rich celestine, barite and dolomite samples from the footwall to the Johnny Lee USZ and dolomite gangue and rhombs from the Lowry and Johnny Lee respectively.

The importance of the Sr values at BBCP is highlighted in Figure 18, where the lowest $^{87}Sr/^{86}Sr$ value of 0.7047 is plotted with the Sr seawater evolution line of Shields and Veizer (2002) at the time of mineralization, about 1.47 Ga (Saintilan et al., 2021). Shields and Veizer (2002) used available Sr-isotope data from marine carbonate rocks to plot a curve summarizing seawater evolution in $^{87}Sr/^{86}Sr$ values through geologic time. Strontianite from the Johnny Lee USZ plots directly on the $^{87}Sr/^{86}Sr$ seawater evolution curve during the time of deposition of the Newland Fm. This portion of the evolution curve is relatively flat, meaning that an initial $^{87}Sr/^{86}Sr$ value near 0.7047 cannot be used to discriminate between 1.47 Ga seawater vs., say, 1.0 Ga seawater. Nevertheless, the data are strong evidence that seawater was the source of Sr at BBCP, and that modified seawater, or connate brines, were a fluid source for mineralization of the Sr-rich samples and dolomite gangue. If magmatic fluids had been involved with the

formation of these minerals, then lower values of $^{87}Sr/^{86}Sr$ would be expected, closer to the mantle evolution line in Figure 18.

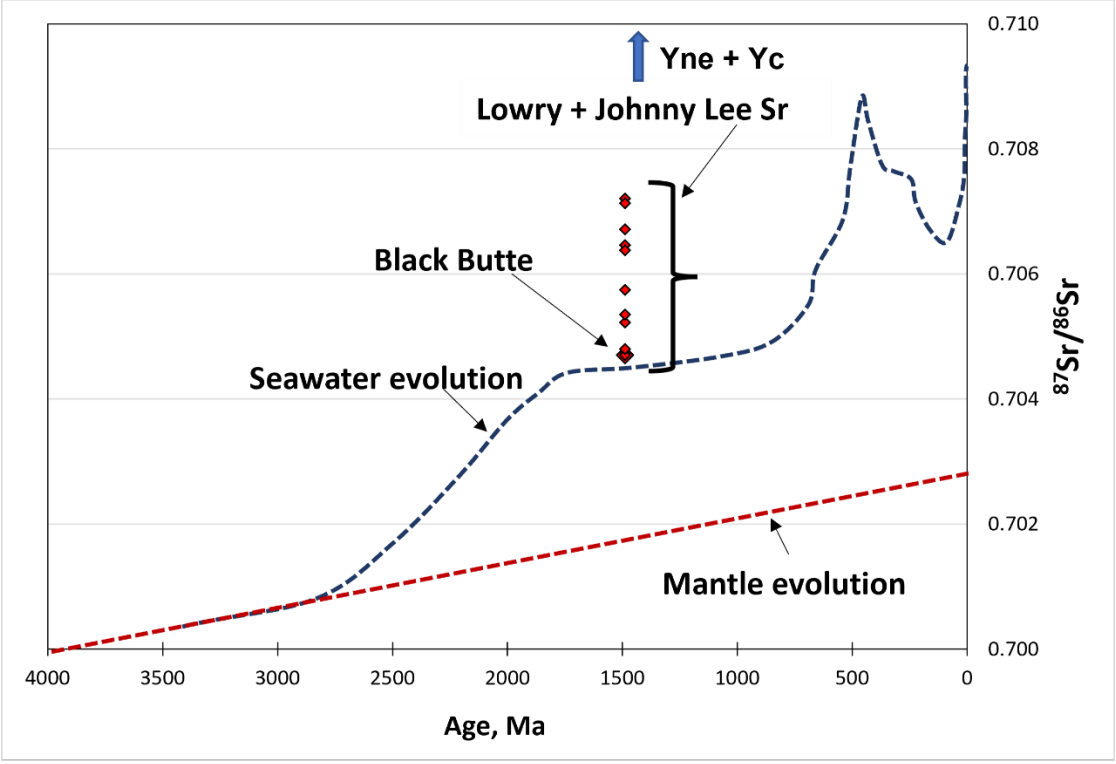

Figure 18: Sr-isotope composition of global seawater (blue dashed line) and the Earth's mantle (red dashed line) vs. geologic time (modified from Shields and Veizer, 2002). The Sr-rich samples from Black Butte plot directly on top of the seawater evolution line, although there is some uncertainty as to the age of the Sr-rich mineralization, here estimated to be 1,488 Ma (Saintilan et al., 2021).

Sr analysis of bulk rock samples from the Neihart and Chamberlain Fms. (Figure 17), which underlie the Newland Fm. and rest atop the Archean granitic gneiss (Figure 5), show a span of $^{87}Sr/^{86}Sr$ values that suggests two end-member Sr sources: 1) a higher initial Rb/Sr source than the Newland Fm. and the Sr-rich minerals from the Lowry and Johnny Lee (Figure 19), likely radiogenic, K-rich clasts, feldspars or micas within the Neihart sandstone and Chamberlain siltstone derived from Archean granitic gneiss; and 2) Belt seawater-like Sr with a lower initial Rb/Sr source that underwent post depositional alteration from the presence of radiogenic materials (Figure 18). There is potential that if specific material within the Neihart

Fm. could be targeted through mineral separation rather than bulk rock analysis, these variable Sr populations could be distinguished.

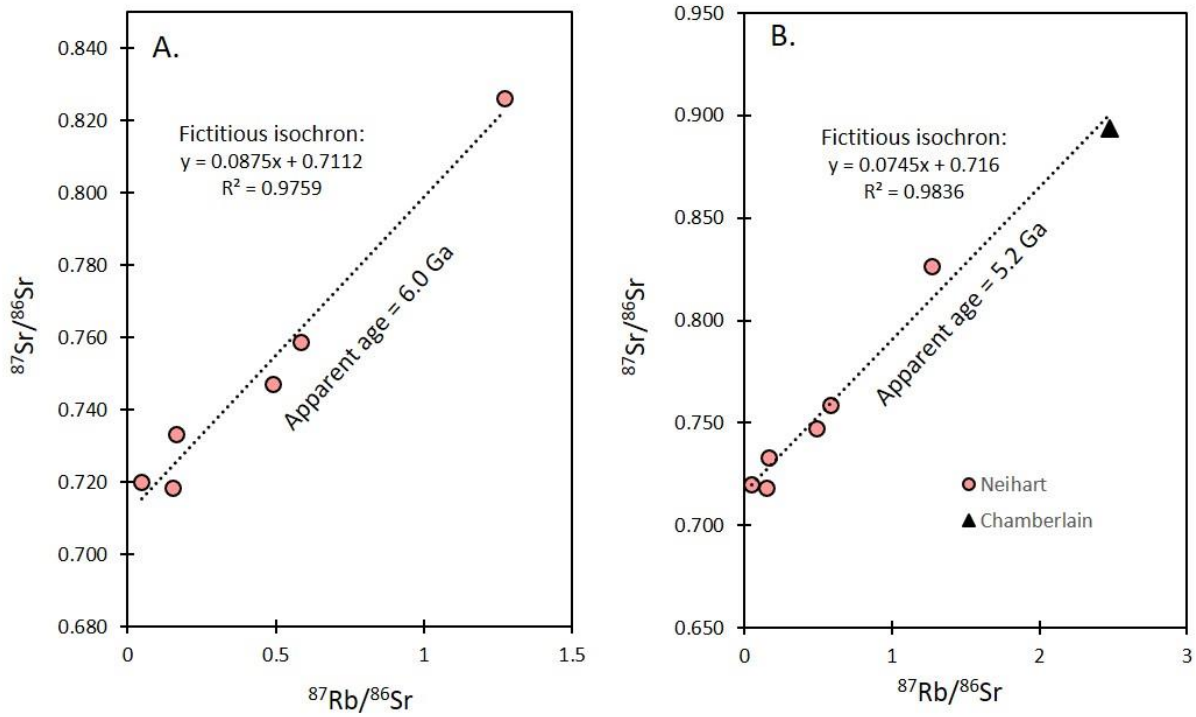

Figure 19: $^{87}Sr/^{86}Sr$ vs. $^{87}Rb/^{86}Sr$ crossplot for samples from A) Neihart Formation; and B) Neihart Fm. + Chamberlain Fm. The linear regressions are "fictitious isochrons" and likely represent mixing of two or more components with different initial Sr and Rb concentrations and isotopic compositions. The apparent ages calculated from the slopes of the lines give meaningless values that are older than the age of the Earth.

4.6. Lead Isotopes

Out of the four stable-Pb isotopes, only ^{204}Pb is non-radiogenic, the other three are the daughter products of uranium and thorium. ^{207}Pb and ^{206}Pb are the daughter products of ^{235}U and ^{238}U respectively, and ^{208}Pb is the daughter product of ^{232}Th. Because the abundance of ^{208}Pb, ^{207}Pb and ^{206}Pb change over time through decay, they are presented as a ratio with the fixed isotope, ^{204}Pb. Like strontium, Pb is incorporated from hydrothermal fluids as a trace or major element into gangue and sulfide minerals (Tosdal et al., 1999). In the absence of U and Th, present day Pb isotope values should reflect the initial composition of ore-forming fluids, and

potentially the metal source, although wall-rock interactions have potential to mix Pb from non-source lithologies (Tosdal et al., 1999).

Figure 19 is a covariation diagram of the thorogenic ($^{208}Pb/^{204}Pb$) and uranogenic lead ($^{207}Pb/^{204}Pb$) from Lowry dolomite and chalcopyrite, along with bedded sulfides from the Sullivan deposit (Beaudoin, 1997), plotted in the plumbo-tectonics model of Zartman and Doe (1981). The plumbo-tectonics model uses the global average of lead isotopes from the associated source rocks throughout Earth history and is used here to characterize the age and source of Pb from the Lowry deposit.

Mineralization at the Sullivan deposit occurred around 1,477 Ma (U-Pb cassiterite geochronology, Slack et al., 2020). Slack et al. (2020) showed evidence for a sedimentary (crustal) source for the metals at Sullivan from the lower Aldridge Fm., which does agree with the modeled Pb source from Zartman and Doe (1981) (Figure 19). Lead from dolomite and chalcopyrite at the Lowry deposit plot much younger along the modeled average crustal growth curve than the known age of chalcopyrite mineralization, ca. 1,488 Ma based on Re-Os chalcopyrite geochronology (Saintilan et al., 2021). Saintilan et al. (2021) also reported an isochron age of 1,358 Ma (Re-Os pyrite geochronology), which they attributed to resetting of the Re-Os system during the ca. 1,370 – 1,325 Ma East Kootenay orogeny (Lydon, 2007). Saintilan et al. (2021) suggested a magmatic source of copper for the BBCP based on primitive Os isotopes. When plotted with the plumbo-tectonics model, Lowry deposit Pb falls under an upper-crustal source.

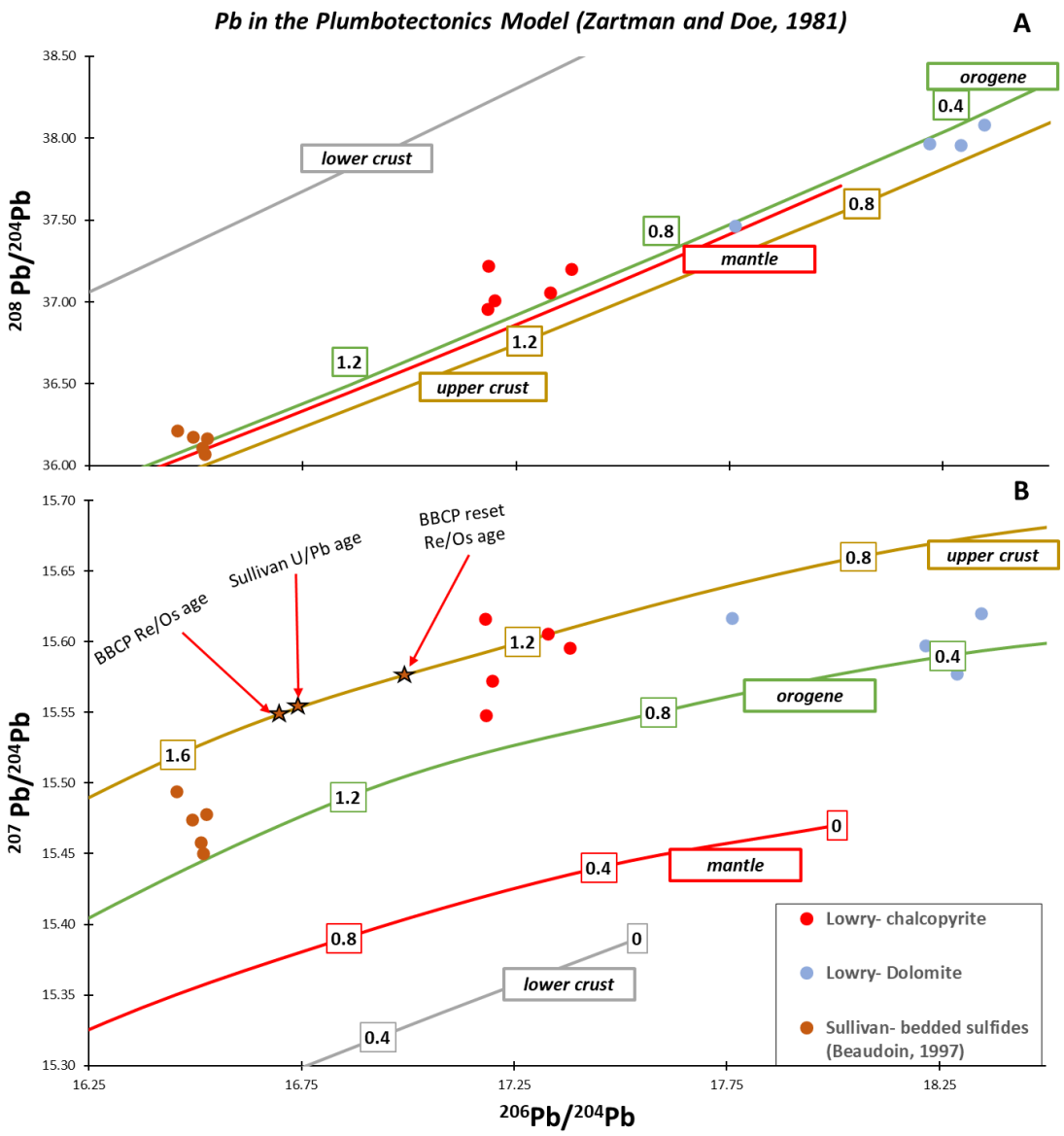

Figure 20: Covariation diagram of thorogenic (A) and uranogenic (B) lead isotopes- Lowry dolomite and chalcopyrite are from this study; BBCP Re/Os ages are from Saintilan et al. (2021); bedded sulfides of the Sullivan deposit are from Beaudoin (1997); U-Pb cassiterite age from Sullivan is from Slack et al. (2020). Ages marked by stars in B. The growth curves from Zartman and Doe (1981) represent average Pb from various crustal material (upper crust, mantle, etc.) through time; highlighted boxes are time in Ga. Isotopic values are not corrected to initial.

The plumbo-tectonics model of Zartman and Doe (1981) suggests that trace Pb from chalcopyrite at the Lowry deposit was sourced from upper crustal material, such as the lower Belt sediment pile or underlying felsic crystalline rocks. The Newland Fm. at the BBCP area

overlies roughly 400 m of Chamberlain siltstone and Neihart quartzite, though these thicknesses increase south of the project area. Emsbo et al. (2016) suggested that a typical Pb-Zn sedimentary-exhalative (sedex) system requires at least 3 km of sediment accumulation to produce the conditions necessary for leaching of metals from basin sediments. While total thickness of the Helena Embayment at the time of mineralization is unknown, The Newland and Greyson achieved a combined thickness of ~6 km basinward (south) of the BBCP (Graham, 2012).

While the environment of mineralization at BBCP is like that commonly described for sedex deposits, the copper (+/- Co-Ni-Ag) content does not reflect the traditional Zn-Pb model of sedex systems (Emsbo et al., 2016), but is more similar to red-bed type copper deposits such as the Kupferschiefer and Central African Copper Belt (Hitzman et al., 2005). White et al. (2014) suggested that the metal source for BBCP was the Neihart Fm., a now clean quartzite that underlies the BBCP. This study tested the Neihart hypothesis through Sr and Pb isotopes as metal tracers (Table 7 – 10) but found little isotopic correlation between the Lowry deposit mineralization and Neihart bulk-rock composition. Although it is now a clean quartzite, it is possible that the Neihart was originally hematitic, but lost its Fe-oxide cement during diagenesis and brine migration. A similar idea has been proposed for the Revett Fm. of the Belt Supergroup, which is host to the Spar Lake, Rock Creek, and Montanore Cu-Ag deposits (Hayes et al., 2012).

The copper content of the BBCP does not fall under the traditional Zn-Pb model of sedex systems but favors the red bed copper model as a metal source. The Neihart sandstone could have acted as a red bed metal source prior to bleaching and would have required much shallower burial depths for metal to be leached from hematite. Although neither Pb nor Sr isotope data

from bulk-rock Neihart samples (Table 8, 10) correlate to the same isotope data for Lowry gangue and sulfides, future studies should target remnant hematite staining in the Neihart to look for isotopic similarities.

4.7. Genetic Model

Figure 20 represents a schematic model for the formation of Lowry deposit and is outlined here. The major control on mineralization style at BBCP is facies type that the ore-forming fluids interacted with. At Johnny Lee, bedded pyrite formed through BSR, and debris flow conglomerates are the dominant facies for mineralization. At Lowry, debris flows and bedded pyrite are also sites for mineralization, but carbonate beds were another important facies that created distinct mineralization styles.

During diagenesis, limestones at the Lowry deposit were altered to dolostone, creating open space for migrating hydrocarbons and fluids. With an increasing thermal regime and the onset of TSR, hydrocarbons were altered to bitumen, sparry dolomite and H_2S. Anhydrite or gypsum could have been dissolved to replenish porewater sulfate or replaced by barite upon interaction with Ba-rich fluids. Hot connate brines migrating up basinal growth faults would have encountered open space in the Lowry and moved laterally, precipitating pyrite, chalcopyrite, and tennantite where they mixed with H_2S-rich pore waters. Precipitation of sulfides would have generated more acidic fluids and led to further dissolution of dolomite to be later precipitated with quartz and sulfides as veins cutting the lower Newland.

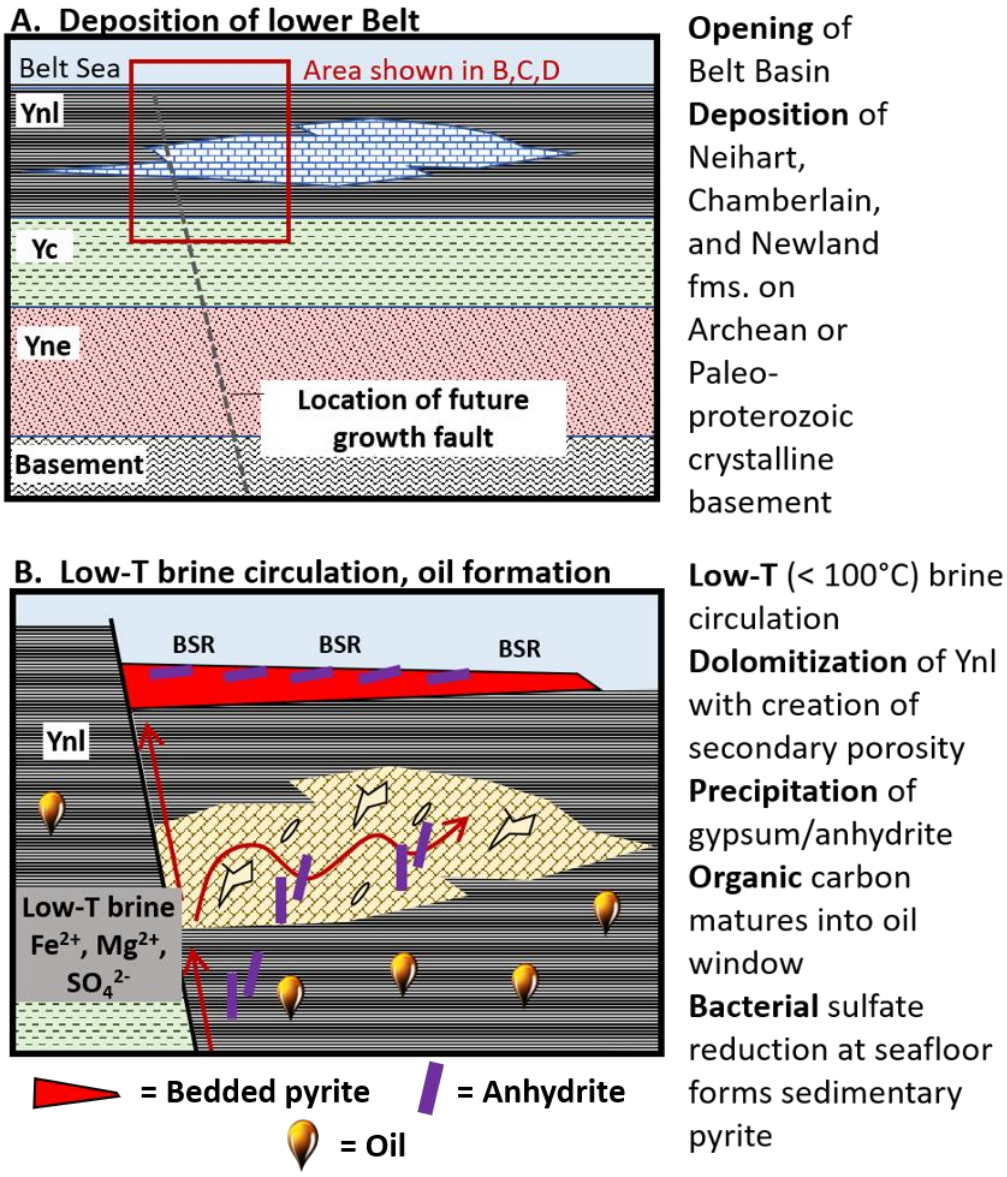

Figure 21: Highly schematic cross sections through BBCP deposits showing differences in facies development that could have led to the variable styles of mineralization. Note that the Johnny Lee and Lowry deposits did not form in the same location as shown here, but within one mile of each other along strike. Not to scale.

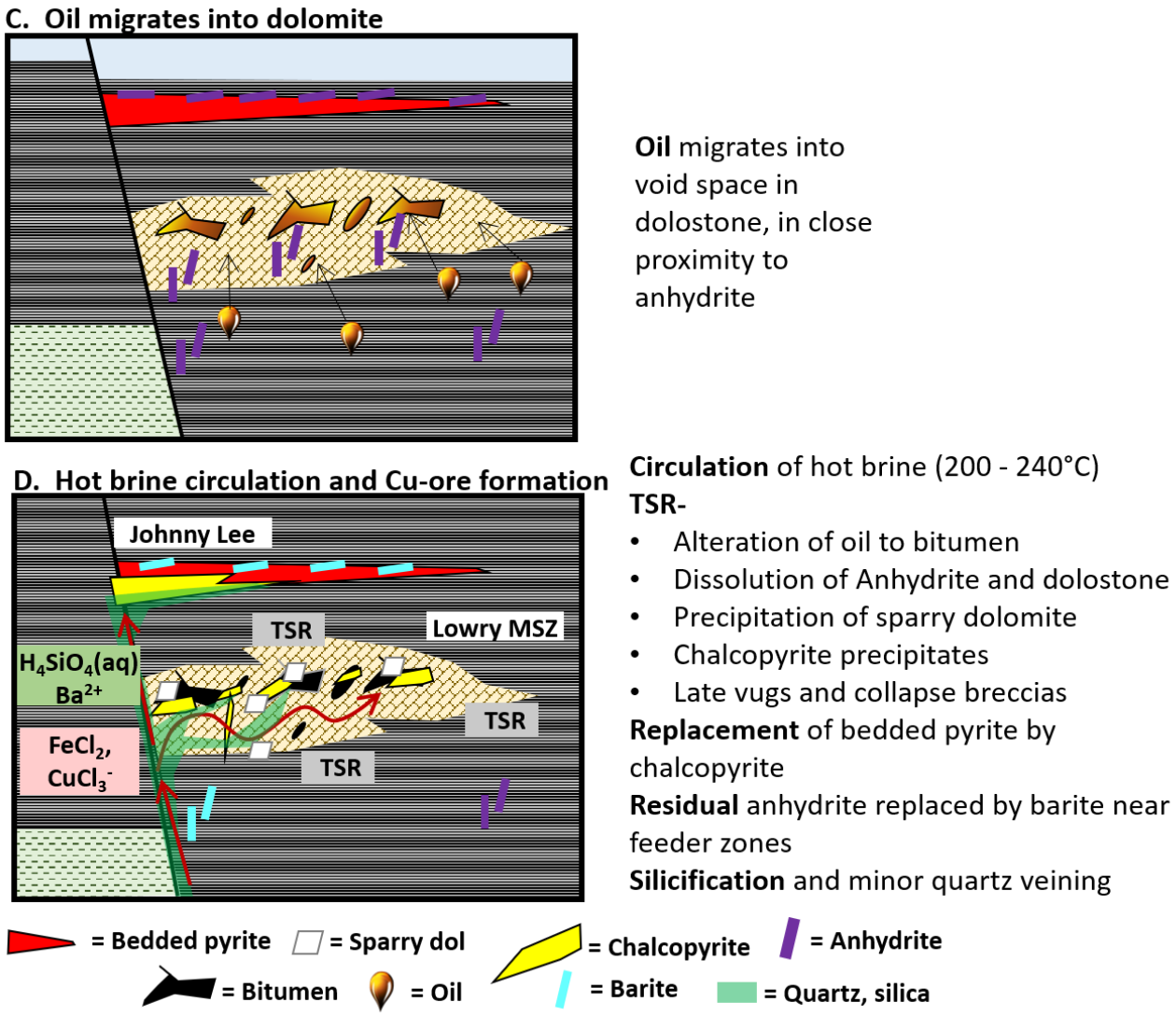

Figure 21: (Continued from previous page). Highly schematic cross sections through BBCP deposits showing differences in facies development that could have led to the variable styles of mineralization. Note that the Johnny Lee and Lowry deposits did not form in the same location as shown here, but within one mile of each other along strike. Not to scale.

5. Conclusions and Recommendations for Future Work

5.1. Conclusions

The following are some of the more important findings and conclusions from this thesis.

- Copper mineralization in the Lowry deposit consists of dominant chalcopyrite +/- tennantite and is associated with multiple stages of pyrite. The dominant gangue in the Lowry deposit is sparry dolomite, followed by quartz and bitumen.
- Mineralization at the Lowry deposit occurred following deposition and diagenesis of the host Newland Fm., as evidenced by cross-cutting veins and reprecipitation of Newland dolomite.
- The $\delta^{34}S$ values of chalcopyrite at Lowry fall between -3.6 to + 3.4 ‰, with a mean of -0.4 ‰ (n=13), similar to the $\delta^{34}S$ values observed for chalcopyrite in the Johnny Lee deposit. This result suggests that chalcopyrite in the Lowry and Johnny Lee deposits share a similar sulfur source, most likely thermochemical reduction of pore-water sulfate.
- Bitumen at the Lowry deposit has a strong association with dolomite, quartz and chalcopyrite. Temperature estimates from bitumen reflectance and RCSM show that the Lowry deposit experienced a mean peak temperature between 223± 8°C (n=8) with a range of 212.8 – 239.5°C and 247± 40°C (n=7) with a range of 219 – 265°C respectively, potentially the temperature of ore-forming fluids.
- Oxygen isotopes of sparry dolomite and Johnny Lee strontianite are depleted relative to bedded dolomite in the host Newland Formation, and fall in the expected range for isotopic equilibrium with Lowry quartz at 220°C. This

suggests that sparry dolomite, strontianite, and quartz at BBCP equilibrated with the same fluid.

- C-isotopes of bitumen are strongly depleted ($\delta^{13}C$ = -30.4 to -33.5‰). Sparry dolomite and strontianite are also depleted in $\delta^{13}C$, suggesting incorporation of light carbon from oxidation of organic matter.

The above findings are consistent with a model in which bitumen at the Lowry deposit was originally liquid petroleum, sourced from maturation of organic carbon in the Newland Fm., that migrated into secondary porosity formed during the dolomitization of the original limestone beds. An increase in temperature during the ore-forming event initiated thermochemical reduction of sulfate to H_2S, resulting in precipitation of chalcopyrite and replacement of early gypsum/anhydrite by sparry dolomite. TSR could have accelerated the degradation of petroleum to bitumen.

New data on the Sr and Pb isotopic composition of gangue and ore minerals leads to the following speculations on the source of the ore fluids at Lowry:

- Sr isotopes in sparry dolomite from the Lowry deposit show a strong association with Sr from Proterozoic seawater, suggesting that ore-forming fluids at the Lowry were sourced from Belt seawater, or obtained Sr through interaction with Newland carbonates prior to dolomite deposition.
- Pb from Lowry dolomite and chalcopyrite fall under an upper-crustal source, suggesting that Pb (and Cu by association) was scavenged from the underlying basin fill and/or crystalline basement.

- Neither the Pb nor the Sr isotopic composition of hydrothermal minerals at Black Butte were shown to correspond closely to values in the Neihart Formation, a possible source rock for the mineralized brines.

The findings of this thesis do not support the idea that high-grade Cu mineralization at Black Butte involved magmatic-hydrothermal fluids. Instead, the ore-forming fluids were most likely connate brines circulating through the Belt Basin. Although Pb-Sr isotope data in this thesis do not directly support the idea that the Neihart Fm. was an important source rock (White et al., 2014), this model should be revisited (see below).

5.2. Recommendations

- The analysis of aromaticity, nitrogen-carbon and sulfur-carbon ratios can be applied to solid bitumen to confirm whether or not the bitumen was a product of thermochemical sulfate reduction (Kelemen et al., 2008). It is recommended that these methods be applied to BBCP bitumen, as this idea has important implications for the timing of deposition of chalcopyrite relative to basin development. As well, it may be possible to directly date bitumen from the Lowry deposit using the Re-Os method (Selby et al., 2005).
- Other possible methods of constraining the temperature of ore formation at Black Butte exist but were not undertaken in this thesis due to time and budgetary constraints. For example, Raman spectroscopy of bitumen in the Cu-rich deposit could be compared with Raman analysis of dispersed organic matter in the Newland Fm. away from areas on known mineralization to determine whether the peak temperatures experienced at Lowry reflect the temperature of Cu mineralization or temperatures obtained during burial metamorphism. In

addition, clumped carbonate-isotope geothermometry (Ghosh et al., 2006) could be used to verify the temperature of formation of sparry dolomite associated with bitumen and chalcopyrite at Lowry.

- As discussed in Section 5.5, the metal source for BBCP remains enigmatic. Multiple authors have suggested a variety of potential metal sources, including syn-rift intrusive igneous rocks (Saintilan et al., 2021), basinal sediments and the underlying crystalline basement (Graham et al., 2012), and the Neihart quartzite (White et al., 2014). This study pursued the hypothesis of White et al. (2014) that copper adsorbed to hematite in the Neihart quartzite could have acted as the metal source. However, Pb and Sr data collected from bulk digestion of the siliclastic sediment of the Neihart may not reflect the isotopic composition of the residual hematite coatings alone. Therefore, it is recommended that hematitic coatings within the Neihart be selectively extracted and analyzed for their Sr and Pb isotope composition.

6. References Cited

Anderson, H. E., & Davis, D. W. (1995). U–Pb geochronology of the Moyie sills, Purcell Supergroup, southeastern British Columbia: implications for the Mesoproterozoic geological history of the Purcell (Belt) basin. *Canadian Journal of Earth Sciences, 32*, 1180–1193. https://doi.org/10.1139/e95-097

Baker, J., Peate, D., Waight, T., and Meysen, C. (2004). Pb isotopic analysis of standards and samples using a ^{207}Pb-^{204}Pb double spike and thallium to correct for mass bias with a double-focusing MC-ICP-MS. *Chemical Geology, 211*, 275–303. http://dx.doi.org/10.1016/j.chemgeo.2004.06.030

Barker, C. E., & Bone, Y. (1995). The minimal response to contact metamorphism by the Devonian Buchan Caves Limestone, Buchan Rift, Victoria, Australia. *Organic Geochemistry, 22*, 151–164. https://doi.org/10.1016/0146-6380(95)90014-4

Beaudoin G. (1997) Proterozoic Pb isotope evolution in the Belt-Purcell Basin: Constraints from syngenetic and epigenetic sulfide deposits. *Economic Geology* 92, 341-350. https://doi.org/10.2113/gsecongeo.92.3.343

Belshaw, N. S., Freedman, P. A., O'Nions, R. K., Frank, M., & Guo, Y. (1998). A new variable dispersion double-focusing plasma mass spectrometer with performance illustrated for Pb isotopes. *International Journal of Mass Spectrometry*, *181*, 51–58. https://doi.org/https://doi.org/10.1016/S1387-3806(98)14150-7

Beyssac, O., Rouzaud, J.N., Goffé, B., Brunet, F., Chopin, C. (2002a). Graphitization in a high-pressure, low-temperature metamorphic gradient: a Raman microspectroscopy and HRTEM study. *Mineralogy and Petrology, 143*, 19–31. https://ui.adsabs.harvard.edu/link_gateway/2002CoMP..143...19B/doi:10.1007/s00410-001-0324-7

Beyssac, O., Goffé, B., Chopin, C., Rouzaud, J.N. (2002b). Raman spectra of carbonaceous material in metasediments: a new geothermometer. *Journal of Metamorphic Geology, 20*, 859–871. https://doi.org/10.1046/j.1525-1314.2002.00408.x

Brown, A. C. (1997). World-class sediment-hosted stratiform copper deposits: Characteristics, genetic concepts and metallotects. *Australian Journal of Earth Sciences*, *44*, 317–328. https://doi.org/10.1080/08120099708728315

Champion, D. C., & Huston, D. L. (2016). Radiogenic isotopes, ore deposits and metallogenic terranes: Novel approaches based on regional isotopic maps and the mineral systems concept. *Ore Geology Reviews*, *76*, 229–256. https://doi.org/10.1016/j.oregeorev.2015.09.025

Chandler, F. W. (2000). The Belt-Purcell Basin as a low-latitude passive rift; implications for the geological environment of Sullivan type deposits: *in Lydon, J.W., Höy, T., Slack, J.F., and*

Knapp, M., eds., Geological Environment of the Sullivan Deposit, British Columbia, Geological Association of Canada, Mineral Deposits Division Special Publication No 1, 82-112.

Cisternas, M. E., & Hermosilla, J. (2006). The role of bitumen in strata-bound copper deposit formation in the Copiapo area, Northern Chile. *Mineralium Deposita*, *41*. https://doi.org/10.1007/s00126-006-0063-9

Clark, I. D., & Fritz, P. (1997). Environmental Isotopes in Hydrogeology (1st ed.). *CRC Press*. https://doi.org/10.1201/9781482242911

Deng, X.-H., Chen, Y.-J., Bagas, L., Zhou, H.-Y., Yao, J.-M., Zheng, Z., & Wang, P. (2015). Isotope (S–Sr–Nd–Pb) constraints on the genesis of the ca. 850Ma Tumen Mo–F deposit in the Qinling Orogen, China. *Precambrian Research*, *266*, 108–118. https://doi.org/https://doi.org/10.1016/j.precamres.2015.05.019

Doughty, P. T., & Chamberlain, K. R. (1996). Salmon River Arch revisited: New evidence for 1370 Ma rifting near the end of deposition in the Middle Proterozoic Belt basin. *Canadian Journal of Earth Sciences*, *33*, 1037–1052. https://doi.org/10.1139/E96-079

Emsbo, P., Seal, R. R., Breit, G. N., Diehl, S. F., & Shah, A. K. (2016). Sedimentary exhalative (sedex) zinc-lead-silver deposit model. *U. S. Geological Survey Scientific Investigations Report 2010-5070N*, 57. https://doi.org/10.3133/sir20105070N

Evans, K.V., Aleinikoff, J.N., Obradovish, J.D., and Fanning, C.M. (2000). SHRIMP U-Pb geochronology of volcanic rocks, Belt Supergroup, western Montana: evidence for rapid deposition of sedimentary strata. *Canadian Journal of Earth Sciences*, *37*, 1287-1300. https://doi.org/10.1139/e00-036

Freeman, W., & Winston, D. W. (1987). A quartz arenite blanket at the base of, or below the middle Proterozoic Belt Supergroup? Montana and Idaho. In *Geological Society of America Abstracts with Programs*, *19*, 276).

Furuichi, H., Ujiie, K., Kouketsu, Y., Saito, T., Tsutsumi, A., & Wallis, S. (2015). Vitrinite reflectance and Raman spectra of carbonaceous material as indicators of frictional heating on faults: Constraints from friction experiments. *Earth and Planetary Science Letters*, *424*, 191–200. https://doi.org/https://doi.org/10.1016/j.epsl.2015.05.037

Ghosh, P., Adkins, J., Affek, H., Balta, B., Guo, W., Schauble, E. A., Schrag, D., & Eiler, J. M. (2006). 13C-18O bonds in carbonate minerals: A new kind of paleothermometer. *Geochimica et Cosmochimica Acta*, *70*, 1439–1456. https://doi.org/10.1016/j.gca.2005.11.014

Giesemann, A., Jager, H. J., Norman, A. L., Krouse, H. P. and Brand, W. A. (1994) On-line sulfur-isotope determination using an elemental analyzer coupled to a mass spectrometer. *Analytical Chemistry*, *66*, 2816-2819. https://doi.org/10.1021/ac00090a005

Gifford, J. N., Mueller, P. A., Foster, D. A., & Mogk, D. W. (2018). Extending the realm of Archean crust in the Great Falls tectonic zone: Evidence from the Little Rocky Mountains, Montana. *Precambrian Research, 315,* 264–281. https://doi.org/10.1016/j.precamres.2018.07.021

Gigon, J., Deloule, E., Mercadier, J., Huston, D. L., Richard, A., Annesley, I. R., Wygralak, A. S., Skirrow, R. G., Mernagh, T. P., & Masterman, K. (2020). Tracing metal sources for the giant McArthur River Zn-Pb deposit (Australia) using lead isotopes. *Geology*, *48*, 478–482. https://doi.org/10.1130/G47001.1

Godlewski, D. W., Zieg, G. A., & Hobbs, S. W. (1984). Stratigraphy and depositional setting of the Precambrian Newland Limestone. *Montana Bureau of Mines and Geology*, *90,* 2-4.

Gammons, C. H. and Zieg, G. A. (2014). Origin of the Black Butte stratiform Cu-Co-Ag massive sulfide deposit, central Montana: Preliminary Sr isotope evidence. *Geological Society of America Abstracts with Programs, 46.*

Graham, G.E., (2012). Geologic and stable isotope investigations of the Sheep Creek Cu-(Co-Ag) deposit and comparison to other sediment-hosted base metal deposits in Mesoproterozoic basins: Unpublished Ph.D. thesis, Golden, Colorado, Colorado School of Mines, 137 p.

Graham, G., Hitzman, M. W. H., & Zieg, J. (2012). Geologic setting, sedimentary architecture, and paragenesis of the Mesoproterozoic sediment-hosted Sheep Creek Cu-Co-Ag deposit, Helena Embayment, Montana. *Economic Geology*, *107*, 1115–1141. https://doi.org/10.2113/econgeo.107.6.1115

Grassineau, N. V., Mattey, D. P., & Lowry, D. (2001). Sulfur isotope analysis of sulfide and sulfate minerals by continuous flow-isotope ratio mass spectrometry. *Analytical Chemistry*, *73*, 220–225. https://doi.org/10.1021/ac000550f

Hackley, P. C., & Lünsdorf, N. K. (2018). Application of Raman Spectroscopy as Thermal Maturity Probe in Shale Petroleum Systems: Insights from Natural and Artificial Maturation Series. *Energy and Fuels*, *32*, 11190–11202. https://doi.org/10.1021/ACS.ENERGYFUELS.8B02171

Hackley, P. C., Araujo, C. V., Borrego, A. G., Bouzinos, A., Cardott, B. J., Carvajal-Ortiz, H., … Jaramillo Zapata, J. E. (2020). Testing reproducibility of vitrinite and solid bitumen reflectance measurements in North American unconventional source-rock reservoir petroleum systems. *Marine and Petroleum Geology*, *114*, 104172. https://doi.org/10.1016/j.marpetgeo.2019.104172

Hall, S. M., and Veizer, J. (1996). Geochemistry of Precambrian carbonates: VII. Belt Supergroup, Montana and Idaho, USA. *Geochimica et Cosmochimica Acta*, *60*, 667-677. https://doi.org/10.1016/0016-7037(95)00424-6

Hayes, T. S., Landis, G. P., Whelan, J. F., Rye, R. O., and Moscati, R. J. (2012). The Spar Lake strata-bound Cu-Ag deposit formed across a mixing zone between trapped natural gas and metals-bearing brine. *Economic Geology*, *107*(6), 1223-1249. https://doi.org/10.2113/econgeo.107.6.1223

Haynes, D. W. (1986). Stratiform copper deposits hosted by low-energy sediments; I, Timing of sulfide precipitation, an hypothesis. *Economic Geology*, *81*(2), 250–265. https://doi.org/10.2113/gsecongeo.81.2.250

Henry, D. G., Jarvis, I., Gillmore, G., & Stephenson, M. (2019). Raman spectroscopy as a tool to determine the thermal maturity of organic matter: Application to sedimentary, metamorphic and structural geology. *Earth-Science Reviews*, *198*, 102936. https://doi.org/10.1016/j.earscirev.2019.102936

Hitzman, M.W., Kirkham, R., Broughton, D., Thorson, J., and Selley, D. (2005), The sediment-hosted stratiform copper ore system: ECONOMIC GEOLOGY 100TH ANNIVERSARY VOLUME, p. 609−642.

Jorgensen B. B. (1979). A theoretical model of the stable isotope distribution in marine sediments. *Geochimica et Cosmochimica Acta*, *43*, 363-374. https://doi.org/10.1016/0016-7037(79)90201-1

Kelemen, S. R., Walters, C. C., Kwiatek, P. J., Afeworki, M., Sansone, M., Freund, H., Pottorf, R. J., Machel, H. G., Zhang, T., Ellis, G. S., Tang, Y., & Peters, K. E. (2008). Distinguishing solid bitumens formed by thermochemical sulfate reduction and thermal chemical alteration. *Organic Geochemistry*, *39*, 1137–1143. https://doi.org/https://doi.org/10.1016/j.orggeochem.2008.04.007

Kelemen, S. R., Walters, C. C., Kwiatek, P. J., Freund, H., Afeworki, M., Sansone, M., Lamberti, W. A., Pottorf, R. J., Machel, H. G., Peters, K. E., & Bolin, T. (2010). Characterization of solid bitumens originating from thermal chemical alteration and thermochemical sulfate reduction. *Geochimica et Cosmochimica Acta*, *74*, 5305–5332. https://doi.org/10.1016/j.gca.2010.06.013

Kelley, K. D., Leach, D. L., Johnson, C. A., Clark, J. L., Fayek, M., Slack, J. F., Anderson, V. M., Ayuso, R. A., & Ridley, W. I. (2004). Textural, compositional, and sulfur isotope variations of sulfide minerals in the Red Dog Zn-Pb-Ag deposits, Brooks Range, Alaska: Implications for Ore Formation. *Economic Geology*, *99*, 1509–1532. https://doi.org/10.2113/gsecongeo.99.7.1509

Kessen, K. M., Woodruff, M. S., & Grant, N. K. (1981). Gangue mineral 87 Sr/ 86 Sr ratios and the origin of mississippi valley-type mineralization. *Economic Geology*, *76*, 913–920. https://doi.org/10.2113/gsecongeo.76.4.913

Landis, C. R., & Castaño, J. R. (1995). Maturation and bulk chemical properties of a suite of solid hydrocarbons. *Organic Geochemistry, 22,* 137–149. https://doi.org/10.1016/0146-6380(95)90013-6

Large, R. R., Bull, S. W. and Winefield, P. R. (2001) Carbon and oxygen isotope halo in carbonates related to the McArthur River (HYC) Zn-Pb-Ag deposit, North Australia: Implications for sedimentation, ore genesis, and mineral exploration. *Economic Geology, 96,* 1567-1593. https://doi.org/10.2113/gsecongeo.96.7.1567

Lonn, J. D., Burmester, R. F., Lewis, R. S., & Mcfaddan, M. D. (2020). The Mesoproterozoic Belt Supergroup. *MBMG Special Publication 122, Geology of Montana*.

Lupoi, J.S., Hackley, P.C., Birsic, E., Fritz, L.P., Solotky, L., Weislogel, A., Schlaegle, S. (2019). Quantitative evaluation of vitrinite reflectance in shale using Raman spectroscopy and multivariate analysis. *Fuel, 254*. https://doi.org/10.1016/j.fuel. 2019.05.156 .

Lünsdorf, N.K., Dunkl, I., Schmidt, B.C., Rantitsch, G. and von Eynatten, H. (2014). Towards a higher comparability of geothermometric data obtained by Raman spectroscopy of carbonaceous material. Part I: evaluation of biasing factors. *Geostandards and Geoanalytical Research, 38*, p. 73-94, doi:10.1111/j.1751908X.2013.12011.x.

Lünsdorf, N.K. and Lünsdorf, J.O. (2016). Evaluating Raman spectra of carbonaceous matter by automated, iterative curve-fitting. *International Journal of Coal Geology, 160*, 51-62. doi:10.1016/j.coal.2016.04.008.

Lünsdorf, N.K., Dunkl, I., Schmidt, B.C., Rantitsch, G. and von Eynatten, H. (2017). Towards a higher comparability of geothermometric data obtained by Raman spectroscopy of carbonaceous material. Part 2: A revised geothermometer. *Geostandards and Geoanalytical Research, 41*, 593-612. doi:10.1111/ggr.12178.

Lydon, J. W. (2007). Geology and metallogeny of the Belt-Purcell basin. *Mineral Deposits of Canada: A Synthesis of Major Deposit-Types, District Metallogeny, the Evolution of Geological Provinces, and Exploration Methods, 5*, 581–607.

Lyons, T. W., Luepke, J. J., Schreiber, M. E., & Zieg, G. A. (2000). Sulfur geochemical constraints on Mesoproterozoic restricted marine deposition: Lower Belt Supergroup, northwestern United States. *Geochimica et Cosmochimica Acta, 64*, 427–437. https://doi.org/10.1016/S0016-7037(99)00323-3

Machel, H. G., Krouse, H. R., & Sassen, R. (1995). Products and distinguishing criteria of bacterial and thermochemical sulfate reduction. *Applied Geochemistry, 10*, 373–389. https://doi.org/10.1016/0883-2927(95)00008-8

Machel, H. G. (2001). Bacterial and thermochemical sulfate reduction in diagenetic settings - old and new insights. *Sedimentary Geology, 140*, 143–175. https://doi.org/10.1016/S0037-0738(00)00176-7

Maghfouri, S., Hosseinzadeh, M. R., Lentz, D. R., Tajeddin, H. A., Movahednia, M., & Shariefi, A. (2021). Nature of ore-forming fluids in the Mehdiabad world-class sub-seafloor replacement SEDEX-type Zn-Pb-Ba-(Cu-Ag) deposit, Iran; constraints from geochemistry, fluid inclusions, and O-C-Sr isotopes. *Journal of Asian Earth Sciences*, *207*, 104654. https://doi.org/10.1016/j.jseaes.2020.104654

Malhotra, D., Ronald, E., Evans, B., and Williamson, P. (2020). Feasibility Study (Johnny Lee Deposit) and Mineral Resource Estimate Update (Lowry Deposit). *Technical Report NI 43-101*.

McMannis, W. J. (1963). LaHood Formation—A coarse facies of the Belt Series in southwestern Montana. *Geological Society of America Bulletin*, *74*, 407–436. https://doi.org/10.1130/0016-7606(1963)74[407:LFCFOT]2.0.CO;2

Movahednia, M., Rastad, E., Rajabi, A., Maghfouri, S., González, F. J., Alfonso, P., Choulet, F., & Canet, C. (2020). The Ab-Bagh Late Jurassic-Early Cretaceous sediment-hosted Zn-Pb deposit, Sanandaj-Sirjan zone of Iran: Ore geology, fluid inclusions and (S–Sr) isotopes. *Ore Geology Reviews*, *121*, 103484. https://doi.org/10.1016/j.oregeorev.2020.103484

MT DEQ (2020). Tintina Resources Inc. Black Butte Copper Project Record of Decision, Montana Department of Environmental Quality. (https://deq.mt.gov/files/Land/Hardrock/Environmental%20Reviews/BlackButteCopperMine_ROD.pdf. Date accessed: January 5th, 2022.

Mueller, P. A., Heatherington, A. L., Kelly, D. M., Wooden, J. L., and Mogk, D. W. (2002). Paleoproterozoic crust within the Great Falls tectonic zone: Implications for the assembly of southern Laurentia. *Geology, 30*, 127-130. https://doi.org/10.1130/0091-7613(2002)030%3C0127:PCWTGF%3E2.0.CO;2

Ohmoto, H. (1996). Formation of volcanogenic massive sulfide deposits: The Kuroko perspective. *Ore Geology Reviews*, *10*, 135–177. https://doi.org/10.1016/0169-1368(95)00021-6

Potra, A., & Moyers, A. (2017). Constraints on the sources of ore metals in Mississippi Valley-type deposits in central and east Tennessee, USA, using Pb isotopes. *Ore Geology Reviews*, *81*, 201–210. https://doi.org/10.1016/j.oregeorev.2016.09.034

Potra, A., Garmon, W. T., Samuelsen, J. R., Wulff, A., & Pollock, E. D. (2018). Lead isotope trends and metal sources in the Mississippi Valley-type districts from the mid-continent United States. *Journal of Geochemical Exploration*, *192*, 174–186. https://doi.org/10.1016/j.gexplo.2018.07.002

Present, T. M., Bergmann, K. D., Myers, C., Slotznick, S. P., Creveling, J. R., Zieg, J., Grotzinger, J. P. (2018). Pyrite-walled tube structures in a Mesoproterozoic sediment-hosted metal sulfide deposit. *Bulletin of the Geological Society of America*, *130*, 598–616. https://doi.org/10.1130/B31504.1

Reynolds, M. W., and Brandt, T. R. (2007). Preliminary geologic map of the White Sulphur Springs 30' X 60' quadrangle, Montana: U. S. Geological Survey.

Riediger, C. L. (1993). Solid bitumen reflectance and Rock-Eval Tmax as maturation indices: an example from the "Nordegg Member", Western Canada Sedimentary Basin. *International Journal of Coal Geology, 22,* 295–315. https://doi.org/10.1016/0166-5162(93)90031-5

Rose, A. W. (1976). The effect of cuprous chloride complexes in the origin of red-bed copper and related deposits. *Economic Geology, 71*(6), 1036-1048. https://doi.org/10.2113/gsecongeo.71.6.1036

Rose, A. W., & Bianchi-Mosquera, G. C. (1993). Adsorption of Cu, Pb, Zn, Co, Ni, and Ag on goethite and hematite; a control on metal mobilization from red beds into stratiform copper deposits. *Economic Geology, 88*(5), 1226-1236. https://doi.org/10.2113/gsecongeo.88.5.1226

Ruiz, J., Richardson, C.K., Patchett, P.J. (1988). Strontium isotope geochemistry of fluorite, calcite, and barite of the Cave-in-rock Fluorite District, Illinois. *Economic Geology, 83,* 203–210.

Saintilan, N. J., Sheldrake, T. E., Creaser, R. A., Selby, D., Zieg, J., Boyce, A., & Chelle-Michou, C. (2021). Synsedimentary to diagenetic Cu ± Co mineralization in Mesoproterozoic pyritic shale driven by magmatic-hydrothermal activity on the edge of the Great Falls tectonic zone–Black Butte, Helena Embayment, Belt-Purcell Basin, USA: Evidence from sulfide Re-Os . *Lithosphere, 2021*, 01–20. https://doi.org/10.2113/2021/7866186

Scher, H. D., E. M. Griffith, and W. P. Buckley (2014). Accuracy and precision of $^{88}Sr/^{86}Sr$ and $^{87}Sr/^{86}Sr$ measurements by MC-ICPMS compromised by high barium concentrations. *Geochemistry, Geophysics, Geosystems, 15*. https://doi.org/10.1002/2013GC005134

Schieber, J. (1989). The origin of the Neihart Quartzite, a basal deposit of the mid-Proterozoic Belt Supergroup, Montana, U.S.A. *Geological Magazine, 126*, 271–281. https://doi.org/10.1017/S0016756800022366

Sears, J. W., Chamberlain, K. R., & Buckley, S. N. (1998). Structural and U-Pb geochronological evidence for 1.47 Ga rifting in the Belt basin, western Montana. *Canadian Journal of Earth Sciences, 35*, 467–475. https://doi.org/10.1139/E97-121

Selby, D., Creaser, R. A., Dewing, K., & Fowler, M. (2005). Evaluation of bitumen as a ^{187}Re-^{187}Os geochronometer for hydrocarbon maturation and migration: A test case from the Polaris MVT deposit, Canada. *Earth and Planetary Science Letters, 235*(1–2), 1–15. https://doi.org/10.1016/j.epsl.2005.02.018

Shields, G., and Veizer, J. (2002) Precambrian marine carbonate isotope database: Version 1.1. Geocehmistry, Geophysics, Geosystems, 3, 1525-2027. https://doi.org/10.1029/2001GC000266

Simbo, C. W., Potra, A., Samuelsen, J. R. (2019). A geochemical evaluation of the genetic relationship between Ouachita mountains Paleozoic rocks and the Mississippi valley-type mineralization in the southern Ozark region, USA. *Ore Geology Reviews, 112*, 103029. http://dx.doi.org/10.1016/j.oregeorev.2019.103029

Singer, D. A. (1995). World class base and precious metal deposits; a quantitative analysis. *Economic Geology*, *90*, 88–104. https://doi.org/10.2113/gsecongeo.90.1.88

Slack, J. F., Neymark, L. A., Moscati, R. J., Lowers, H. A., Ransom, P. W., Hauser, R. L., & Adams, D. T. (2020). Origin of tin mineralization in the Sullivan Pb-Zn-Ag deposit, British Columbia: Constraints from textures, geochemistry, and LA-ICP-MS U-Pb geochronology of cassiterite. *Economic Geology*, *115*(8), 1699–1724. https://doi.org/10.5382/econgeo.4761

Slotznick, S.P., Zieg, J., Webb, S.M., Kirschvink, J.L., and Fischer, W.W. (2015). Iron mineralogy and redox chemistry of the Mesoproterozoic Newland Formation in the Helena Embayment, Belt Supergroup, Montana. *Northwest Geology*, *44*, 55–72

Stacey, J. S., & Kramers, J. D. (1975). Approximation of terrestrial lead isotope evolution by a two-stage model. *Earth and Planetary Science Letters*, *26*(2), 207–221. https://doi.org/10.1016/0012-821X(75)90088-6

Strauss, H., and Schieber, J. (1990). A sulfur isotope study of pyrite genesis: The mid-proterozoic Newland formation, belt supergroup, Montana. *Geochimica et Cosmochimica Acta*, *54*, 197–204. https://doi.org/10.1016/0016-7037(90)90207-2

Taylor, H., (1979) Oxygen and hydrogen isotopes in hydrothermal mineral deposits. In Barnes, H. L. (ed.), *Geochemistry of Hydrothermal Ore Deposits, 2nd ed.* Wiley: New York, NY, 509-567.

Tosdal, R.M., Wooden, J.L., Bouse, R.M. (1999). Pb isotopes, ore deposits, and metallogenic terranes. *Reviews in Economic Geology, 12*, 1–28.

Tucker, M. E., Wright, V. P., Dickson, J. A. D. (1990). Carbonate Sedimentology. *Blackwell Science.*

Vho, A., Lanari, P., Rubatto, D. (2020) An internally-consistent database for oxygen isotope fractionation between minerals. *Journal of Petrology 60*, 2101-2129. https://doi.org/10.1093/petrology/egaa001

Weis, D., Kieffer, B., Maerschalk, C., Barling, J., de Jong, J., Williams, G.A., Hanano, D., Pretorius, W., Mattielle, N., Scoates, J.S., Goolaerts, A., Friedman, R.M., Mahoney, J.B. (2006). High-precision isotopic characterization of USGS reference materials by TIMS and

MC-ICP-MS. *Geochemistry, Geophysics, Geosystems, 7*. https://doi.org/10.1029/2006GC001283

White, B. G. (2016). Unkinking the Lewis and Clark tectonic zone, Belt Basin, Idaho and Montana. In J. S. MacLean & J. W. Sears (Eds.), *Belt Basin: Window to Mesoproterozoic Earth, Geological Society of America, 522*. https://doi.org/10.1130/2016.2522(13)

White J (2012) Paragenesis of cobalt and nickel at the Black Butte Copper Project, Meagher County, Montana. *M.S. thesis, Montana Technological University, Butte, Montana*.

White, J., Gammons, C. H., and Zieg, G. A. (2014). Paragenesis of cobalt and nickel in the Black Butte shale-hosted copper deposit, Belt Basin, Montana, USA. *Mineralium Deposita, 49*, 335–351. https://doi.org/10.1007/s00126-013-0492-1

White, W.M., Albarède, F., Télouk, P. (2000). High-precision analysis of Pb isotope ratios by multi-collector ICP-MS. *Chemical Geology, 167*, 257-270. https://doi.org/10.1016/S0009-2541(99)00182-5

Winston, D. (1986). Middle Proterozoic tectonics of the Belt Basin, western Montana and northern Idaho. in Roberts, S.M., ed., *Belt Supergroup: A guide to Proterozoic rocks of western Montana and adjacent areas: Montana Bureau of Mines and Geology Special Publication 94*, 238-245.

Winston, D. (1989). A sedimentologic and tectonic interpretation of the Belt Supergroup. In Hanshaw, P. M., ed., Volcanism and Plutonism of Western North America; Volume 2, Middle Proterozoic Belt Supergroup, Western Montana, *Field trips for the 28th International Geological Congress, American Geophysical Union, Winston, D., Horodyski, R.J., and Whipple, J.W., leaders*, 47-70.

Winston, D., and Link, P. (1993). Middle Proterozoic rocks of Montana, Idaho and eastern Washington: The Belt Supergroup, in Reed, J.C., Jr., Bickford, M.E., Houston, R.S., Link, P.K., Rankin, R.W., Sims, P.K., and Van Schmus, W.R., eds., Precambrian: Conterminous U.S. Boulder, Colorado, Geological Society of America, *The Geology of North America, C-2* , p. 487–517.

Wooden, J. L., Vitaliano, C. J., Koehler, S. W., and Ragland, P. C. (1978). The late Precambrian mafic dikes of the southern Tobacco Root Mountains, Montana: geochemistry, Rb-Sr geochronology and relationships to Belt tectonics. *Canadian Journal of Earth Sciences, 15*, 467–479. https://doi.org/10.1139/e78-055

Xiao, Z., Gammons, C. H., & Williams-Jones, A. E. (1998). Experimental study of copper (I) chloride complexing in hydrothermal solutions at 40 to 300°C and saturated water vapor pressure. *Geochimica et Cosmochimica Acta, 62*, 2949-2964. https://doi.org/10.1016/S0016-7037(98)00228-2

Zartman, R. E., and Stacey, J. S. (1971) Lead isotopes and mineralization ages in Belt Supergroup rocks, northwestern Montana and northern Idaho. *Economic Geology* 66, 849-860. https://doi.org/10.2113/gsecongeo.66.6.849

Zartman, R. E., & Doe, B. R. (1981). Plumbotectonics—the model. *Tectonophysics*, *75*(1), 135–162. https://doi.org/https://doi.org/10.1016/0040-1951(81)90213-4

Zheng Y.F. (1999). Oxygen isotope fractionation in carbonate and sulfate minerals. *Geochemical Journal, 33*, 109-126. https://doi.org/10.2343/geochemj.33.109

Zieg, G. A. (1986). Stratigraphy and Sedimentology of the Middle Proterozoic upper Newland Limestone. In S.M. Roberts (Ed.), Belt Supergroup. *Montana Bureau of Mines and Geology, Special Publication, 94*, 125-141.

Zieg, G. A., & Lietch, C. H. (1998). The Geology of the Sheep Creek Copper Deposits, Meagher County, Montana. In *Belt Symposium III (Comp. R. Berg) Abstracts Montana Bureau of Mines and Geology Open File Report* (Vol. MBMG 381).

Zieg, G., Scartozzi, V., Chutas, N., Albers, D., Gostomski, K., Jones, J. (2013). Black Butte Copper Deposits, lower Belt Supergroup, Montana. *Northwest Geology, 48*, 131-148.

7. Appendix

7.1. Appendix A: Notes on Sr-rich samples from Johnny Lee deposit

Prior to this thesis, samples of Sr-rich drill core from the base of the Upper Sulfide Zone at the Johnny Lee deposit were sent to MTU for petrography and isotopic analysis. Two samples, which came from drill hole SC12-120 at a depth of 146 to 146.3m, were sent to the University of Wyoming for C- and O-isotope analysis of carbonate (mainly $SrCO_3$) and to the University of Waterloo for $^{87}Sr/^{86}Sr$ analysis. Representative photographs and microphotographs are given in Figures AX and AY below. Strontianite ($SrCO_3$), celestine ($SrSO_4$), and Sr-rich barite occur as veinlets and coatings in massive pyrite, and are associated with quartz, pyrite, chalcocite, bornite, and minor amounts of calcite. Chalcopyrite is notably absent from the Sr-rich assemblage, although it is present in the surrounding massive pyrite.

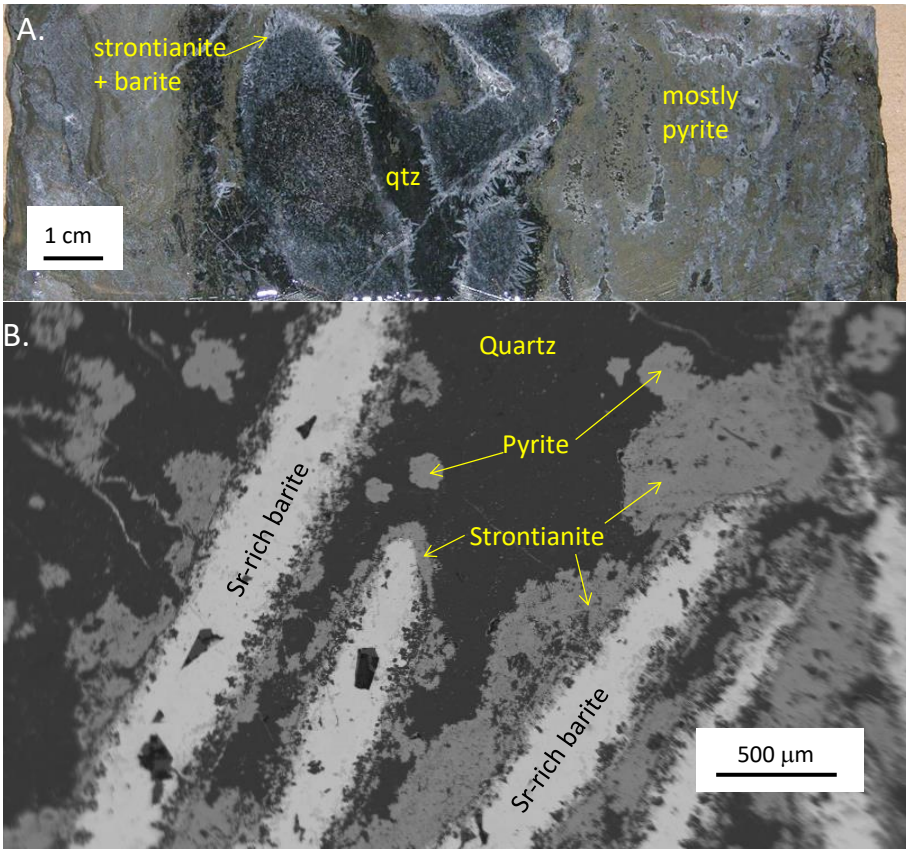

Figure A-A 1: Sr-rich sample from SC12-120, 146m. A) drill core photo; B) SEM-BSE image.

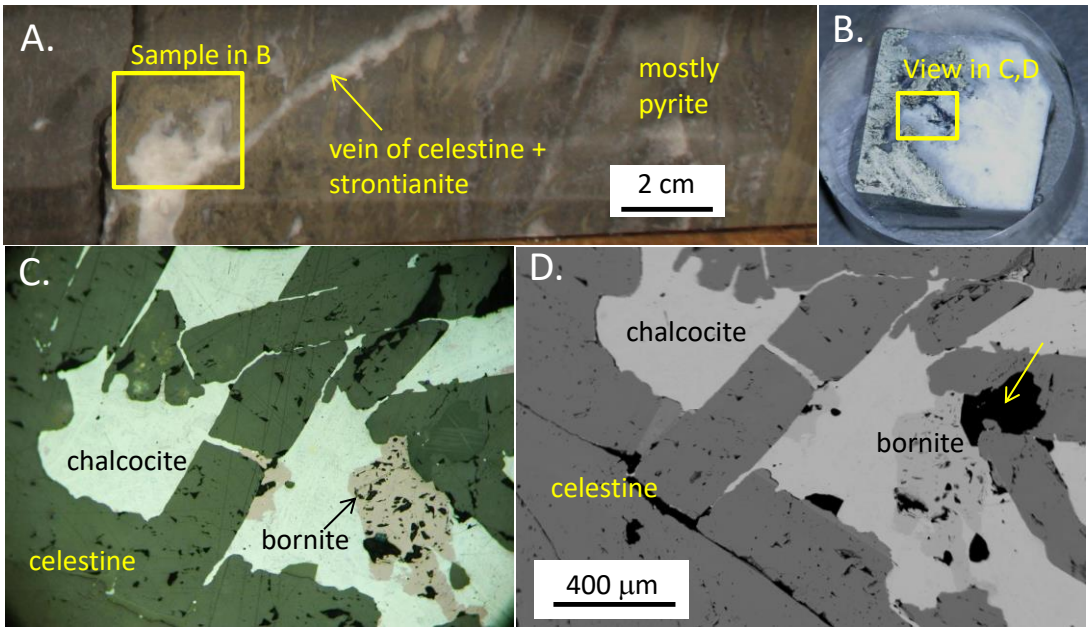

Figure A-A 2: Sr-rich sample from SC12-120, 146.3m. A) drill core photo; B) polished plug; C) reflected light photo; D) SEM-BSE image.

7.2. Appendix B: Bitumen Reflectance Images

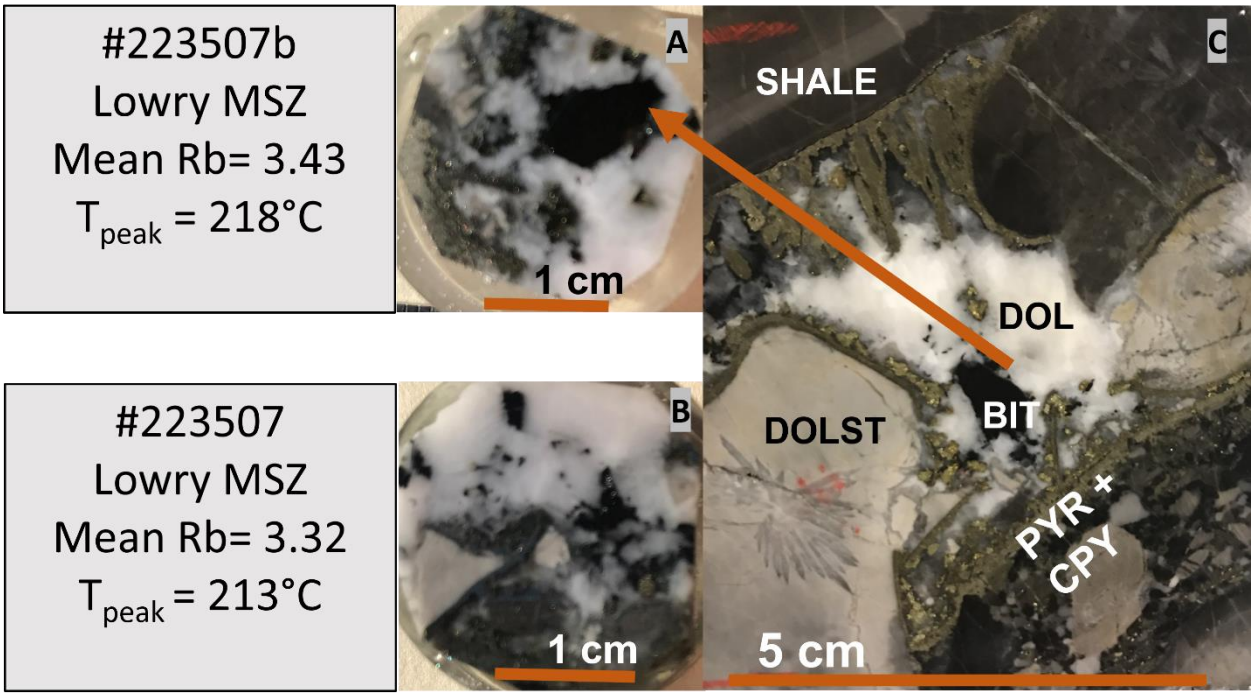

Figure A-B 1: Example of samples for bitumen reflectance analysis showing two plugs (A, B) made from sample SC12-160-395.62 (C). Reflectivity values from this sample produced mean peak temperature estimates of 213 and 218°C. Bit- bitumen, dol- dolomite, dolst- dolostone, pyr + cpy- pyrite and chalcopyrite

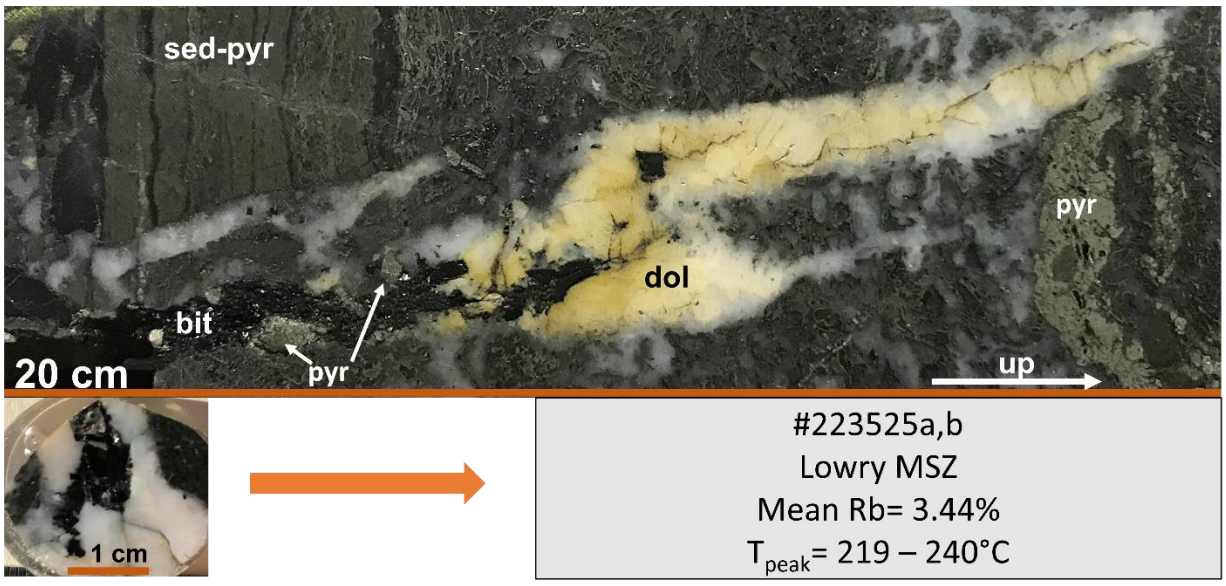

Figure A-B 2: Example of sample for bitumen reflectance analysis from sample SC12-157-419.24. Reflectivity values from two plugs of this sample produced mean peak temperature estimates of 219 and 240°C. Bit- bitumen, dol- dolomite, pyr- pyrite, sed-pyr- sedimentary pyrite.